Remodeling the zonula adherens in response to tension and the role of afadin in this response

Wangsun Choi,[1] Bipul R. Acharya,[4*] Grégoire Peyret,[5*] Marc-Antoine Fardin,[5*] René-Marc Mège,[5] Benoit Ladoux,[5,6] Alpha S. Yap,[4] Alan S. Fanning,[2,3] and Mark Peifer[1,2]

[1]Department of Biology, [2]Lineberger Comprehensive Cancer Center, and [3]Department of Cell Biology and Physiology, University of North Carolina at Chapel Hill, Chapel Hill, NC 27599
[4]Division of Cell Biology and Molecular Medicine, Institute for Molecular Bioscience, The University of Queensland, St. Lucia, Queensland, Australia 4072
[5]Institut Jacques Monod, Centre National de la Recherche Scientifique UMR 7592 and Université Paris Diderot, 75013 Paris, France
[6]Mechanobiology Institute, National University of Singapore, Singapore 117411, Singapore

Morphogenesis requires dynamic coordination between cell–cell adhesion and the cytoskeleton to allow cells to change shape and move without losing tissue integrity. We used genetic tools and superresolution microscopy in a simple model epithelial cell line to define how the molecular architecture of cell–cell zonula adherens (ZA) is modified in response to elevated contractility, and how these cells maintain tissue integrity. We previously found that depleting zonula occludens 1 (ZO-1) family proteins in MDCK cells induces a highly organized contractile actomyosin array at the ZA. We find that ZO knockdown elevates contractility via a Shroom3/Rho-associated, coiled-coil containing protein kinase (ROCK) pathway. Our data suggest that each bicellular border is an independent contractile unit, with actin cables anchored end-on to cadherin complexes at tricellular junctions. Cells respond to elevated contractility by increasing junctional afadin. Although ZO/afadin knockdown did not prevent contractile array assembly, it dramatically altered cell shape and barrier function in response to elevated contractility. We propose that afadin acts as a robust protein scaffold that maintains ZA architecture at tricellular junctions.

Introduction

Epithelia are the most common tissue architecture, underlying organs as diverse as skin, colon, and kidney. During development and homeostasis, epithelial cells undergo dramatic changes in shape and motility while maintaining tissue integrity (Harris and Tepass, 2010), and alterations in this process underlie many birth defects and help drive cancer metastasis. Cell shape change is powered by the actomyosin cytoskeleton, but to alter cell shape, the contractile machinery must link to the plasma membrane via cell–cell junctions or cell–matrix adhesions.

In the original textbook view, the cell–cell zonula adherens (ZA) is a ring of transmembrane cadherins linked to an underlying ring of actin and myosin via β- and α-catenin (Meng and Takeichi, 2009). Cell junctions and the cytoskeleton are mutually reinforcing, with cadherin complexes regulating junctional actin assembly and actin stabilizing junctions (Gumbiner et al., 1988; Quinlan and Hyatt, 1999). Work in the last decade revealed that cell junctions respond dynamically to their environment, with built-in tension sensors measuring force exerted on junctions and initiating cytoskeletal reorganization. For example, applied force alters α-catenin conformation, revealing a binding site for the actin-binding protein vinculin (Yonemura et al., 2010; Yao et al., 2014). Thus antibodies to vinculin or α-catenin's open conformation (α18) can help reveal where contractile force is exerted on junctions. Most recently, Leerberg et al. (2014) identified a feedback loop by which contractility stimulates ZA actin polymerization, which in turn increases epithelial cadherin (Ecad) recruitment, reinforcing both junctions and their actomyosin connections.

During morphogenesis, cells generate and respond to tension as they change shape and move. This must occur without disrupting epithelial barrier function or tissue integrity. Studying this process provided new insights into the nature of junctional–cytoskeletal connections. For example, apical constriction requires a contractile actomyosin network across the apical surface, with a "clutch" to engage cell junctions (Martin et al., 2009; Roh-Johnson et al., 2012). Convergent extension

*B.R. Acharya, G. Peyret, and M.-A. Fardin contributed equally to this paper.

Correspondence to Mark Peifer: peifer@unc.edu; Alan Fanning: fanningalan@gmail.com; or Wangsun Choi: wchoi@email.unc.edu

W. Choi's present address is Dept. of Pathology and Dept. of Medicine, Brigham and Women's Hospital and Harvard Medical School, Boston, MA 02115.

Abbreviations used in this paper: BCJ, bicellular junction; DIL, dilute; Ecad, epithelial cadherin; ICC, immunocytochemistry; KD, knockdown; MCJ, multicellular junction; MRLC, myosin regulatory light chain; PIV, particle image velocimetry; RA, Ras association; ROCK, Rho-associated, coiled-coil containing protein kinase; SIM, structured-illumination microscopy; TCJ, tricellular junction; TER, trans-epithelial resistance; TJ, tight junction; WB, Western blotting; ZA, zonula adherens; ZO, zonula occludens.

The Rockefeller University Press $30.00
J. Cell Biol. Vol. 213 No. 2 243–260
www.jcb.org/cgi/doi/10.1083/jcb.201506115

requires an even more elaborate setup: both actomyosin contractility and junctional proteins are planar polarized along the plane of the epithelium (Vichas and Zallen, 2011). These data focused attention on the cellular "unit of contractility" during tissue reorganization, highlighting that individual cells can endow adjacent cell–cell bicellular borders with distinct contractile properties. Even during seemingly isotropic apical constriction, distinct cell borders respond to tension differentially (Martin et al., 2010). Mathematical modeling built on this new view of individual cell borders, joined at vertices, as the unit of cell shape change, providing a theoretical underpinning for these data (Fletcher et al., 2014).

One candidate cytoskeletal–junction linker to help maintain tissue integrity in response to the contractility driving shape change is afadin/Canoe (Miyamoto et al., 1995; Mandai et al., 1997). This multidomain scaffolding protein binds diverse cytoskeletal and junctional proteins. *Drosophila melanogaster* Canoe plays roles in apical constriction, convergent extension, and collective cell migration (Sawyer et al., 2009, 2011; Choi et al., 2011). Based on these roles, we proposed that Canoe links the ZA to the cytoskeleton: in its absence, actomyosin detaches from the ZA, disrupting morphogenesis. Afadin may have similar roles; mutant mice have defects in gastrulation (Ikeda et al., 1999; Zhadanov et al., 1999), kidney lumen formation (Yang et al., 2013), and intestinal barrier function (Tanaka-Okamoto et al., 2011). However, tissue complexity in vivo limits the ability to draw mechanistic conclusions.

We thus used a simple epithelial model to explore this issue. Zonula occludens (ZO) family proteins are important apical contractility regulators (Fanning et al., 2012). Best known for roles in barrier function at tight junctions, ZO proteins also play tissue-specific roles in ZA assembly (Ikenouchi et al., 2007). Knockdown (KD) of ZO-1 plus ZO-2, the predominant family members in MDCK cells, dramatically altered the ZA, with assembly of a robust contractile actomyosin network accompanied by cell border straightening (Fanning et al., 2012). These cells thus provided a model to explore how cells remodel the ZA in response to elevated contractility. We used superresolution microscopy to examine ZA remodeling in molecular detail and examine how changes in individual cells alter the architecture and properties of the entire epithelial sheet. In parallel, we explored how cells balance elevated contractility with tissue integrity, revealing a striking role for afadin.

Results

Bicellular junctions are individual contractile units whose tension is increased by ZO KD

Confluent epithelial cells are linked together by a network of cell–cell junctions. For clarity, we will refer to junctions between two adjacent cells as bicellular junctions (BCJs) and those at the contacts between three or more junctions as tricellular junctions (TCJs) or multicellular junctions (MCJs). Effectively, BCJs intersect at TCJs.

We previously found that ZO proteins regulate actomyosin arrays at the ZA of BCJs (Fanning et al., 2012). After ZO-1/ZO-2 KD in MDCK cells (ZO KD; Fig. S1 A), F-actin and myosin IIB (Fig. 1, C vs. D) assemble into a prominent apical contractile network at the ZA (as does myosin IIA), and the curvilinear junctions of control monolayers are replaced by very straight cell borders (Fig. 1, A vs. B and C). Individual ZO KD cells apically constrict when placed in a monolayer of control cells (Fanning et al., 2012), suggesting that contractility is increased. To verify this, we measured the instantaneous recoil of BCJs marked by Ecad–GFP after laser ablation. Indeed, ZO KD substantially increased initial recoil velocity (Fig. 1 F). Assuming that viscous drag is a minor contributor to recoil in these morphologically homogeneous cultures, this result implies that contractile tension at BCJs is increased by ZO KD. However, although ZO KD cells pull on one another, tension is well balanced among cells of the sheet.

This increase in contractility was associated with strikingly dynamic behavior of the BCJs. When imaged with GFP-tagged myosin regulatory light chain (MRLC-GFP; Video 1; Fig. 1, H and I; and Fig. S1 B), we found that individual BCJs displayed periods of shortening (Fig. 1 H, green and yellow arrows) and elongation (Fig. 1 H, red and blue arrows), and neighboring borders could undergo simultaneous but opposite changes in border length (Fig. 1 H, cell 2 green border shrinks whereas red border elongates; cell 3, yellow border shrinks whereas blue border elongates). Thus the BCJs appeared to behave as individual contractile units.

Despite the dynamic contractile behavior of individual BCJs, ZO KD cells remained polygonal and relatively constant in the apical area (Fig. S1, C and D) and had a more uniform major/minor axis aspect ratio than control cells (Fig. 1 E). Further, particle imaging velocimetry (PIV) applied to videos of cultured cells (see Materials and methods; Vedula et al., 2012) revealed that overall cell movement within monolayers was reduced by ZO KD (Videos 2 and 3; and Fig. 1 G, mean velocity 8.85 µm/h in controls vs. 5.62 µm/h in ZO KD). This observation may be related to the increased contractility of ZO KD cells at BCJs that could lead to a balanced tension across the tissue and restrain cell movement. Together, these data suggest that ZO KD is a useful model to test how cells maintain tissue integrity under tension and, in particular, how they may remodel their junctions to achieve this end.

ZO KD increases contractility via a Shroom and Rho kinase pathway

To define how ZO KD increased contractility, we examined the role of Rho-associated, coiled-coil containing protein kinase (ROCK; Julian and Olson, 2014). Although 24-h treatment with ROCK inhibitors did not reverse myosin accumulation after ZO KD (Fanning et al., 2012), we suspected that long-term treatment might elicit compensatory responses. Consistent with this hypothesis, actomyosin arrays were completely abolished after 20-min treatment with the ROCK inhibitor Y27632 (Fig. S2 A), and this was accompanied by the linear borders of ZO KD cells becoming more curvilinear (Fig. S2, B vs. C). This result implicated ROCK in stimulating myosin assembly and contractility upon ZO KD.

Several different pathways can recruit or regulate ROCK at the ZA. These include Par3, which can negatively regulate ROCK by recruiting aPKC/Par6 to the ZA (Ishiuchi and Takeichi, 2011), and aPKC itself, which can inhibit junctional actin assembly via Lulu2 (Nakajima and Tanoue, 2011). However, ZO KD actually slightly increased junctional aPKC and Par3 (Fig. S2, F–I), which would be predicted to inhibit ROCK-dependent contractility, the exact opposite of what we observed. Thus ROCK recruitment after ZO KD is not dependent on reduced junctional aPKC. Shroom proteins can also mediate

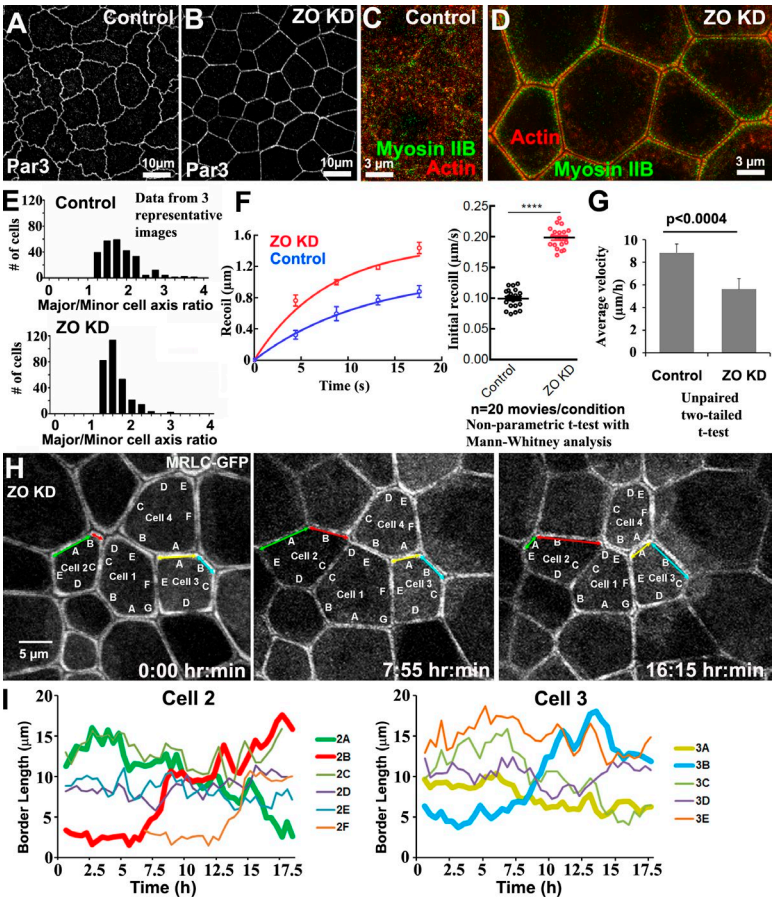

Figure 1. **ZO KD elevates contractility, and individual bicellular borders fluctuate independently.** (A and B) ZO KD in MDCK cells straightens junctions. (C and D) SIM and actomyosin architecture. (E) Major/minor axis aspect ratios. ZO KD leads to more isotropic cell shapes. (F) Laser-cutting cell junctions. Left, recoil over time; right, mean initial recoil velocity. Error bars are SDs of the data from a minimum of 30 contacts from three independent experiments. (G) Mean cell velocity calculated using velocity fields obtained by PIV analysis of phase-contrast videos. Error bars are SDs of the data from a minimum of 300 cells from three independent videos. (H) Live imaging of MRLC-GFP–expressing ZO KD cells. Highlighted borders are discussed in text. (I) Quantification of the length of indicated borders of cells 2 and 3. Individual bicellular borders expand and contract independently.

ROCK recruitment to cell junctions (Nishimura and Takeichi, 2008). Although Shroom3 was diffusely cytoplasmic in control cells (Fig. 2 A), ZO KD led to strong elevation at the ZA (Fig. 2 B). Furthermore, transient Shroom3 overexpression in control cells led to ROCK recruitment to the ZA (Fig. 2 C) and could drive assembly of a robust ZA actomyosin network similar to that assembled after ZO KD (Fig. 2 D). Conversely, we found that Shroom3 siRNA reduced junctional F-actin and increased apical cell area in ZO KD cells (Fig. 2, F and G), suggesting that Shroom is necessary to increase apical contractility in ZO KD cells.

Afadin is recruited to the ZA after ZO KD and is essential to maintain tissue homogeneity

We next used ZO KD cells to address how cells maintain tissue integrity in the face of elevated contractility and how junctions are remodeled to ensure this. The ZA scaffolding protein afadin is required during fly embryogenesis for cell shape change and morphogenetic movement without tissue disruption. We hypothesized that afadin might play a similar role in the response when BCJ tension is increased in MDCK cells. Strikingly, afadin was significantly increased at the ZA after ZO KD, at BCJs (Fig. 3, A and B; greater than threefold), and especially at TCJs (Fig. 3 C′, arrow) and MCJs (Fig. 3 C′, arrowheads). Interestingly, fly Canoe is also enriched at TCJs (Sawyer et al., 2009).

We then stably depleted afadin by shRNA in control or ZO KD cells (protein levels <10% controls, with little change in expression of other junctional or cytoskeletal proteins; Fig. S1, A and E). Afadin KD alone subtly affected cell shape, with slight cell border straightening but no substantial changes in cortical Ecad, ZO-1, or myosin (Fig. 3, D–G; and not depicted). However, afadin KD in ZO KD cells (ZO/afadin KD) dramatically altered cell shape (Fig. 4, A vs. B). Although individual cell borders remained straight, cell shapes became highly irregular, with many cells very elongated along one axis (Fig. 4, C [arrows], D, and E). Intriguingly, groups of cells often elongated in parallel (Fig. 4 C), pointing toward MCJs, where several adjacent cell borders were hyperconstricted (Fig. 4 C, arrowheads); these resemble the multicellular rosettes formed during fly convergent extension (Blankenship et al., 2006). These changes in cell shape were rescued by reexpressing RNAi-resistant afadin (Fig. S1 F). Thus afadin regulates cell shape in cells with elevated contractility.

This impression was reinforced and amplified by live cell imaging. Phase-contrast imaging revealed that ZO/afadin KD cells displayed large-scale patterns of movement transmitted long distances across the monolayer, contrasting with the much more local patterns of cell movement in control or ZO KD monolayers (Video 4). Quantification revealed a substantial increase in cell velocity (Fig. 4 F) and velocity correlation length (Fig. 4 G) relative to control or ZO KD, suggesting that larger groups of cells moved together. To further analyze collective dynamics, we used data from our phase-contrast movies, defining cell centroids and computing the divergence ($\nabla.v$) of the velocity field throughout the monolayer, where positive values corresponded to regions of expansion and negative values to regions of contraction (Fig. 4 H). This clearly showed that ZO/afadin KD cells exhibited large-scale coherent patterns of spreading and contracting regions spanning hundreds of micrometers (Fig. 4 H, correlation

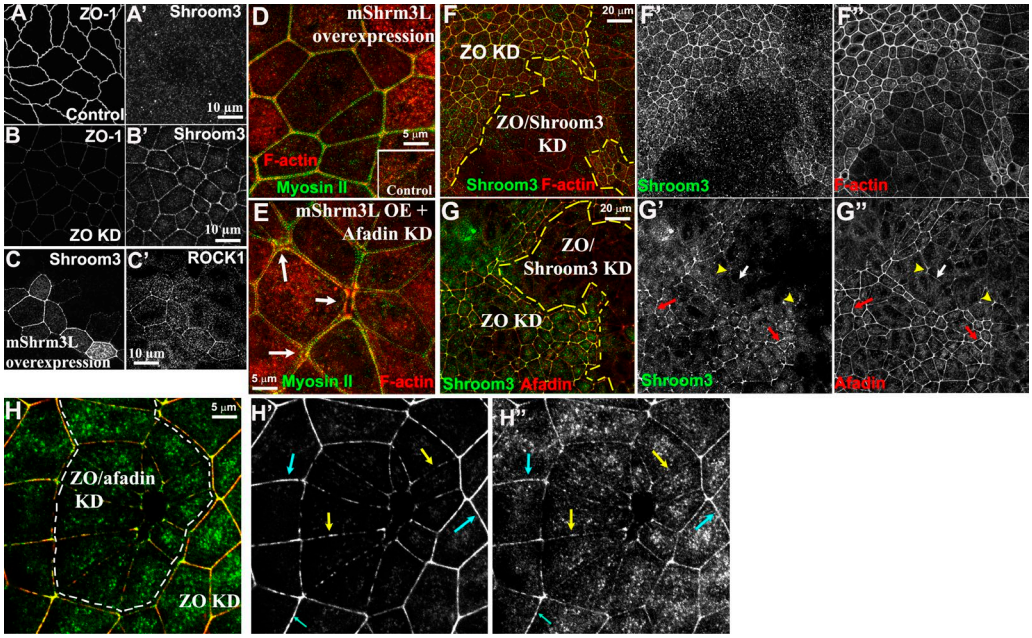

Figure 2. **Shroom3 is recruited to the ZA in response to ZO KD and stimulates actomyosin contraction.** (A and B) Control versus ZO KD cells. ZO-1 and Shroom3 are shown. (C) Control cells or cells expressing murine Shroom3L cocultured. Shroom3 and ROCK1 are shown. (D) mShroom3L overexpression in MDCK cells led to ZA actomyosin assembly and border straightening. (E) Afadin KD in mShroom3L-overexpressing cells. ZA actomyosin assembled, but defects were seen at MCJs (arrows). (F and G) ZO KD cells transiently transfected with siRNA targeting canine Shroom3. Shroom3, afadin, and F-actin are shown. Cells with reduced Shroom3 (F′ and G′) have reduced F-actin and afadin and larger apical areas. (H) ZO KD and ZO/afadin KD cells cocultured. ZO/afadin KD cells have less uniform Shroom3 at the ZA.

curves) as opposed to control and ZO KD, which exhibited more homogeneous divergence maps. Individual ZO/afadin KD cells were also highly dynamic, with rapid cell shape changes (Fig. S3 A, green and blue cells; and Video 5), formation of rosette-like cell arrangements (Fig. S3 A, around yellow cell; and Video 6), and areas where cells regained columnar epithelial character (Fig. S3 B and Video 7). It is important to note the caveat that we assessed cell shape and tissue architecture dynamics in monolayers with architecture that is already severely disrupted, complicating the assessment of cause and effect.

The centers of cell rosettes seen after ZO/afadin KD were associated with ZA discontinuities (manifested as reduced apical Ecad; Fig. 4 B, asterisks and green arrows). These did not represent gaps in the monolayer, as a myosin network remained. Instead, 3D rendering of the apical regions of the monolayer showed that they represented abnormal variation in cell height. Both control and afadin single KD cells form monolayers of uniform cell height and flat surface morphology (Fig. 5, A, C, and E [magenta arrow]). ZO KD cells were taller, with distended apical surfaces (Fig. 5, B and F), but they retained a uniform height (Fig. 5 F, magenta arrow). In contrast, cell height was extremely variable after ZO/afadin KD (Fig. 5, D and G). Some cells had very pronounced apical constriction and were even taller than those in ZO KD (Fig. 5, D and G, arrowheads; and Fig. S4, long magenta arrows), whereas others were much shorter and less columnar (Fig. 5, D and G, arrows; and Fig. S4, short magenta arrows). Thus the ZA "gaps" in the most apical regions of ZO/afadin KD monolayers coincide with these extremely short cells. Consistent with this finding, although the tallest cells retained strong ZA actomyosin similar to ZO KD cells (Fig. 5, F vs. G arrowheads), the shortest cells had actin and myosin stretched over the "top" of the cell (Figs. 5 G and S4, blue arrows), likely representing the stretched actomyosin network seen in larger gaps (Fig. 4 B, green arrows). Thus ZO/

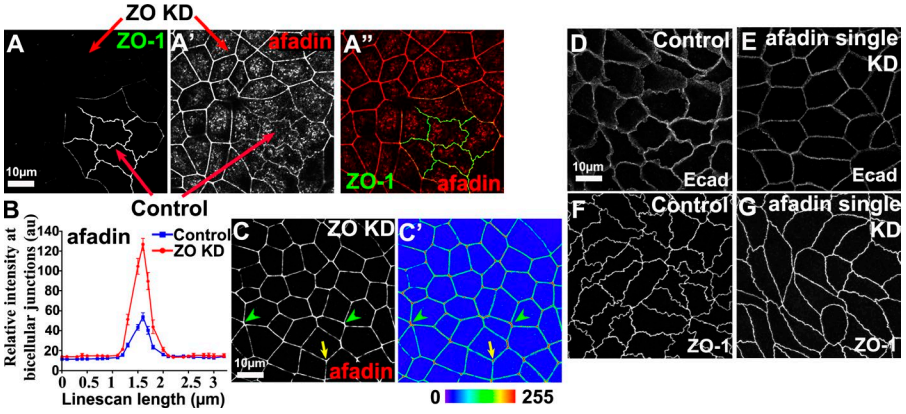

Figure 3. **ZO KD elevates afadin at the ZA.** (A) Control and ZO KD cells cocultured. ZO-1 marks control cells. Junctional afadin increases after ZO KD. (B) Line scans from cocultures (10/image, three images). Error bars are SDs. Mean afadin intensity at BCJs is higher after ZO KD. au, arbitrary unit. (C) Afadin is enriched at TCJs (arrow) and MCJs (arrowheads). (C′) Spectrum display of image intensity. (D–G) Junctional ZO-1 or Ecad unchanged by afadin single KD.

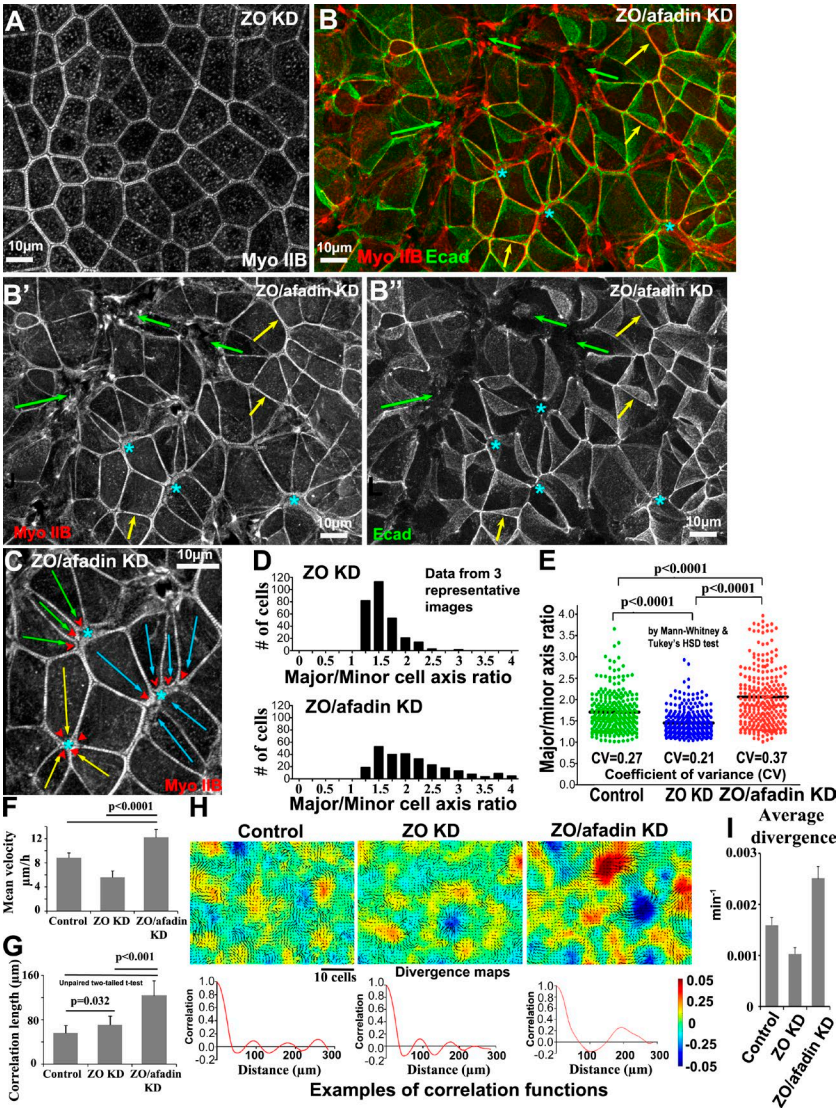

Figure 4. **Afadin KD dramatically alters the shape of ZO KD cells.** (A–C) ZO KD versus ZO/afadin KD (A vs. B). (B) At many BCJs, the myosin array was unaltered (yellow arrows), but rosette-like cell arrangements pointing toward sets of hyperconstricted junctions (C, arrows and arrowheads) and areas of reduced or disrupted apical Ecad staining (asterisks and green arrows) were observed in other areas. (B and C) Maximum-intensity projections (5-μm apical) covering apical half of the tissue. (D) Major/minor axis aspect ratios. Note shift from isotropic to elongated in ZO/afadin KD. (E) Scatter plot of axis ratios. Both mean and coefficient of variance (CV) were significantly higher in ZO/afadin KD. (F) Mean velocity calculated based on velocity field (v) via PIV analysis of phase-contrast videos. (G) Spatial correlation of velocity fields. (H) Heat maps of divergence fields ($\nabla.v$) superimposed to cell velocity fields showing coherent patterns of extending (positive, red) and contracting (negative, blue) regions. The correlation curves of the divergence field below the heat maps represent the distance over which divergence patterns extend or contract. (I) Histogram of the mean magnitude of divergence. In F, G, and I, error bars are SDs of 300 cells (n = 3).

afadin KD affected both individual cell shape and monolayer morphology but did not prevent cells from assembling an intact epithelium. This suggested that afadin KD disrupted the ability of ZO KD cells to maintain tissue homogeneity.

ZO/afadin KD does not fragment the epithelium or prevent cell sheet contractility

To analyze how afadin maintained tissue homeostasis after ZO KD, we first examined patterns of tension in the monolayers. We considered the possibility that contractility of individual BCJs might be altered when afadin was depleted in ZO KD cells. Accordingly, we laser-ablated individual BCJs, comparing control, ZO KD, and ZO/afadin KD, along with ZO/afadin KD cells rescued by reexpressing full-length afadin (Fig. 5 H). Supposing that the dramatic variation in BCJ length might represent substantial changes in tension, in each case we separately cut either short (<6 μm) or long (>6 μm) borders. As noted earlier, instantaneous recoil was increased by ZO KD, in both short and long borders. This was slightly reduced in long borders of ZO/afadin KD cells but was not affected in short borders, and was fully restored by reexpressing afadin (Fig. 5 H). This result suggested that the elevated contractility of BCJs in ZO KD cells was not substantively affected by afadin KD, although it must be noted that variation in cell shape makes it difficult to infer tension from recoil measurements.

It was possible, however, that changes that were not apparent at the level of individual BCJs might be amplified at the tissue/monolayer level. To test whether tissue contractility was altered, we gently detached monolayers from the substrate with dispase (Fig. 5 I). Control cell sheets remain flat and loosely attached to the substrate, suggesting minimal tension within the cell sheet (Fig. 5 I, left). In contrast, ZO KD cell sheets remained intact but retracted from the substrate, forming a cup-like shape (Fig. 5, I [middle] and J), consistent with increased BCJ tension. The myosin inhibitor blebbistatin restored flat cell sheets (Fig. 5 I, middle). Thus myosin contractility in individual ZO KD cells is transmitted throughout the sheet. Interestingly, ZO/afadin KD epithelial sheets also remained intact and contracted when detached from the substrate (Fig. 5, I [right] and K), and blebbistatin inhibited this (Fig. 5 I, right). This result implied that afadin KD did not compromise tissue-level contractility in ZO KD cells.

ZO KD triggers assembly of a robust actomyosin network at the ZA

To define in molecular detail how the ZA was remodeled in response to elevated contractility, we combined superresolution

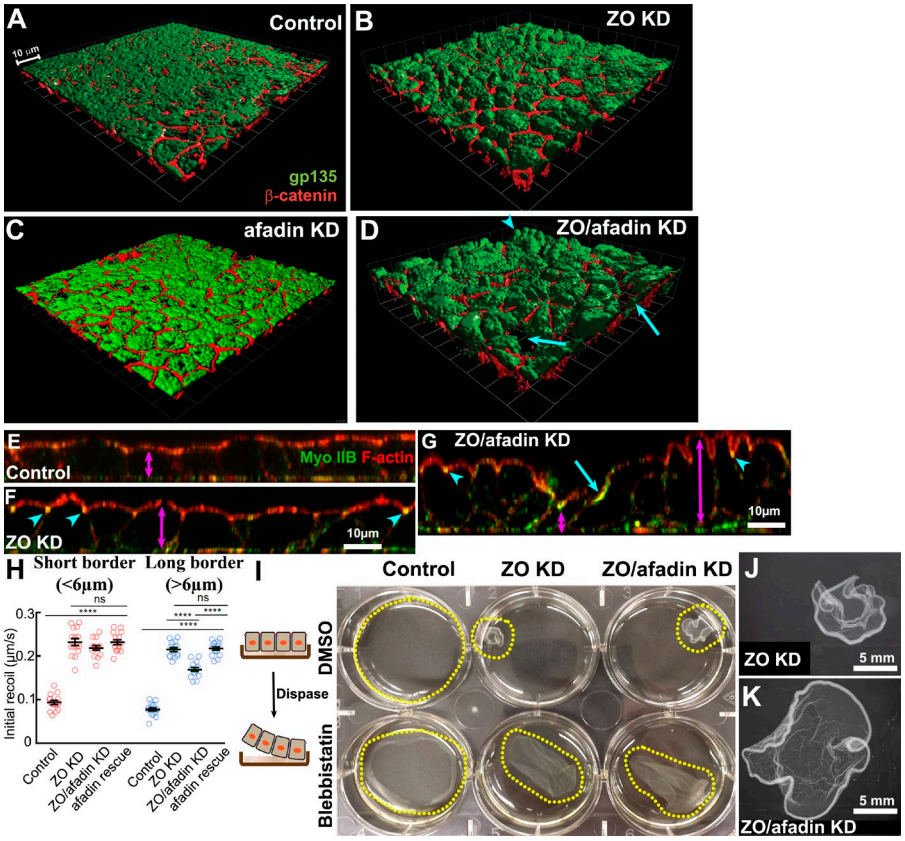

Figure 5. **ZO/afadin KD does not fragment monolayers or prevent tissue contractility.** (A–D) 3D rendering of the whole tissue section (A–C, 10 µm; D, 15 µm) or cross sections (E–G) of control, ZO KD, afadin single KD, or ZO/afadin KD monolayers. Glycoprotein 135 (gp135) marks the apical surface. Control (A and E) and afadin single KD (C) monolayers have flat surfaces and uniform cell height (E, double arrow). ZO KD cells (B and F) are domed and slightly taller (F, double arrow) and have ZA actomyosin (arrowheads). ZO/afadin KD cells (D and G) vary from very tall and domed (arrowheads and right double arrow) to very short and not columnar (arrows and right double arrow). (H) Laser cutting of long (>6 µm) or short (<6 µm) borders. Error bars are SDs of >30 contacts (n = 3). ns, not significant. (I, left) Schematic of monolayer detachment by dispase. (right) DMSO (control) or 0.1 mM blebbistatin treatment. Control monolayer remains flat, whereas ZO KD and ZO/afadin KD monolayers are constricted. Blebbistatin relaxed constriction. (J and K) Higher magnification image of I.

light microscopy via structured illumination (SIM) with transmission electron microscopy (EM), extending our earlier confocal analysis (Fanning et al., 2012). We examined the cytoskeleton and Ecad. Control cells do not have a prominent ZA, exhibiting a loosely organized junctional F-actin network interspersed with microvilli (Fig. 6 B). In contrast, ZO KD cells assemble a highly ordered ZA actomyosin array (Fig. 6, A and C). This is associated with Ecad puncta (Fig. 7, A and B, arrows) recruited into a pronounced apical ZA (Fig. S5, B [inset] and C), which contrasts with the control cells, in which Ecad localizes all along basolateral membranes with only subtle apical enrichment (Fig. S5 A, inset). Actin assembled into continuous cables at the ZA (Fig. 6 C), with ∼70 nm separating cables of adjacent cells. EM indicated that these actin cables at BCJs tightly associate with the plasma membrane (Fig. 6 E; Fanning et al., 2012). Myosin IIB was organized along these ZA actin cables in periodic linear structures perpendicular to the membrane, with a mean spacing of 415 nm (Fig. 6 C), like the ZA sarcomeric array of auditory hair cells but without the actin periodicity seen there (Ebrahim et al., 2013). Expressing MRLC-GFP and costaining with myosin heavy chain tail antibodies suggested a head-tail-head myosin minifilament orientation (Fig. 6 F). Thus ZO KD triggers assembly of a strikingly ordered actomyosin array at the ZA along BCJs.

Bicellular F-actin cables anchor end-on at tricellular junctions

TCJs act as the endpoints of the independently contractile BCJs observed after ZO KD, and also were the sites of ZA disruption after ZO/afadin KD. We thus examined their architecture. After ZO KD, spacing between F-actin bundles in adjacent cells increased slightly at TCJs (Fig. 6 D, arrow). SIM and EM revealed that rather than creating gaps between cells, ZO KD alters ZA structure and F-actin orientation relative to the plasma membrane at TCJs. SIM revealed striking Ecad elevation at TCJs (Fig. 7, A and C; and Fig. S5 B, arrowheads), with Ecad occupying the membrane proximal space between F-actin bundles (Fig. 7, A and B, arrowheads). EM revealed that these BCJ F-actin filaments of ZO KD cells appeared to terminate end-on at TCJ/MCJs. Interestingly, these termination points (Fig. 6, H and H″, green arrows) coincided with kinks in the plasma membrane (Fig. 6, H [brackets] and H′), suggestive of forces being exerted by the bundles, which contrasted with the smooth membranes of control cells (Fig. 6 G). These data suggest that actomyosin arrays along individual BCJs are separate contractile units that anchor end-on in the ZA near TCJs.

Afadin is not essential for BCJ cable assembly or anchoring to the membrane but is essential to maintain the ZA at TCJs

To probe mechanisms by which afadin acts, we expanded our superresolution analysis to ZO/afadin KD cells. We considered three hypotheses: (1) afadin is essential to assemble BCJ actomyosin arrays, (2) afadin globally maintains junctional–cytoskeletal linkage, and (3) afadin strengthens the ZA at places where tension is highest.

Despite dramatic effects of ZO/afadin KD on cell shape, afadin KD did not reverse the elevated ZA actomyosin at BCJs (Fig. 6, I [yellow arrows] and J). Many BCJs remained unchanged after ZO/afadin KD, with strongly elevated parallel actin bundles closely associated with opposed plasma membranes, highly periodic myosin (Fig. 6, J and K), and Ecad puncta lining BCJs (Fig. 7, D and E, yellow arrows). Dual-imaging myosin heavy chain tail and MRLC-GFP suggested that

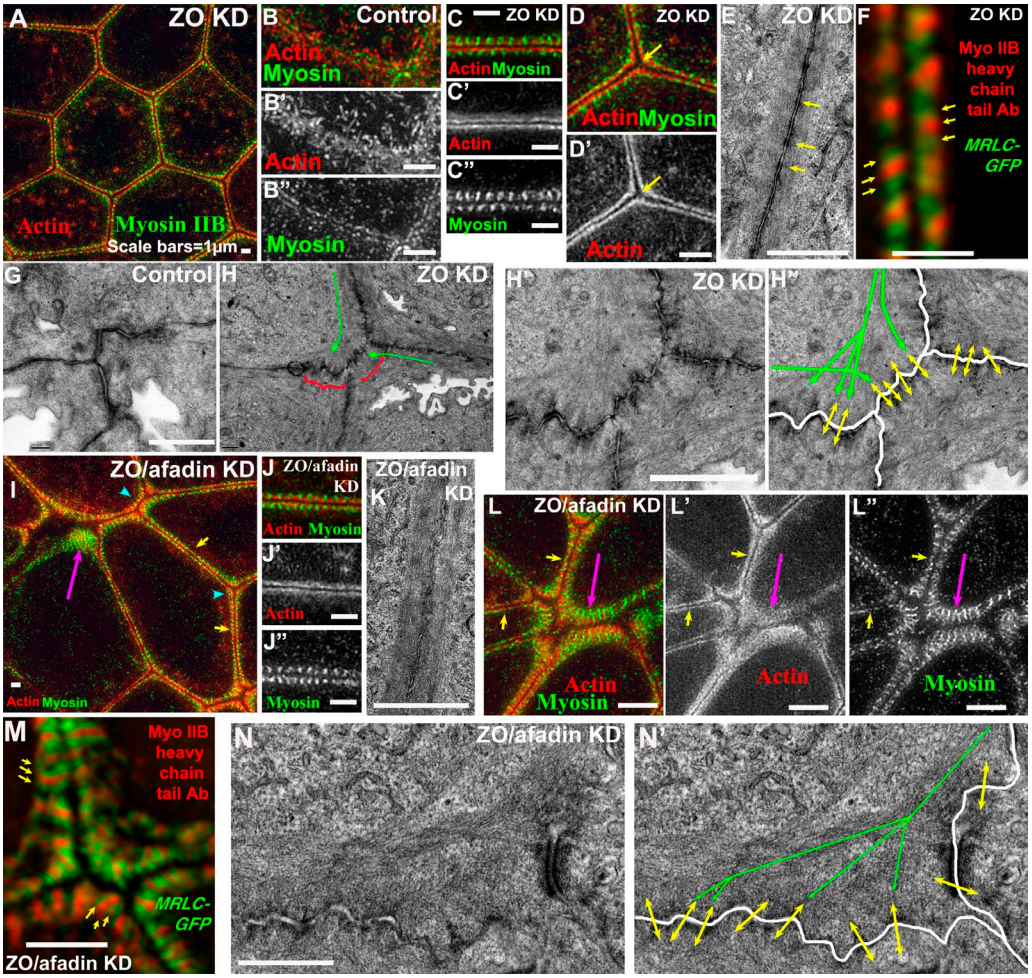

Figure 6. **Superresolution views of ZA remodeling in response to elevated contractility, and afadin's role in this response.** (A–D′, F, I, J″, L, and M) SIM of actomyosin and projections of apical 2-µm sections. (E–H, K, and N) EM, en face sections. (A–E) At BCJs, ZO KD cells assemble bundled actin cables decorated with periodic myosin structures absent in control—space between cables increases at TCJs (D, arrow). EM reveals periodic densities along BCJ cables (E, arrows). Myosin heavy chain antibodies plus MRLC-GFP reveal myosin minifilament polarity (F, arrows). (G and H) EM suggests that after ZO KD (H), actin cables spread apart as they reach TCJs (green arrows) and anchor end-on at junctions, leading to membrane folding (brackets and double arrows) not seen in control (G). (I–N) ZO/afadin KD. Actomyosin at BCJs (I, L [yellow arrows], J, and K) and some TCJs (arrowheads in I) is largely unchanged, but at many TCJs and MCJs, actin forms a more diffuse network, and periodic myosin structures expand laterally (I, L [magenta arrows], and M). Polarity of myosin minifilaments is unchanged (M, arrows). (N) EM reveals actin cables spread out and membrane remains folded near TCJs of ZO/afadin cells. Bars, 1 µm.

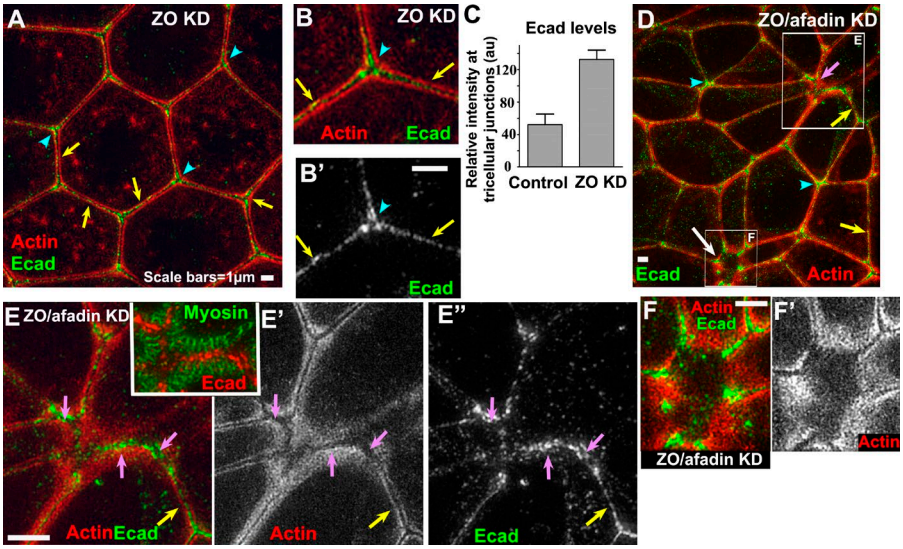

Figure 7. **ZO KD leads to Ecad enrichment at tricellular junctions.** (A, B, and D–F) SIM projections of apical 2-µm sections. (A–C) ZO KD. Ecad puncta are scattered along BCJs (arrows) and enriched at TCJs, where they fill spaces between actin cables (C, arrowheads). Error bars are SDs of >30 tricellular contacts (n = 3). (D–F) ZO/afadin KD. Ecad puncta remain scattered along BCJs (yellow arrows) and enriched at TCJs (arrowheads), but at MCJs (magenta arrows) where actin becomes diffuse and myosin structures expand laterally, Ecad puncta fill spaces in these networks (E). At larger scale, ZA discontinuities (D [white arrow] and F) and Ecad surrounds the region. Bars, 1 µm.

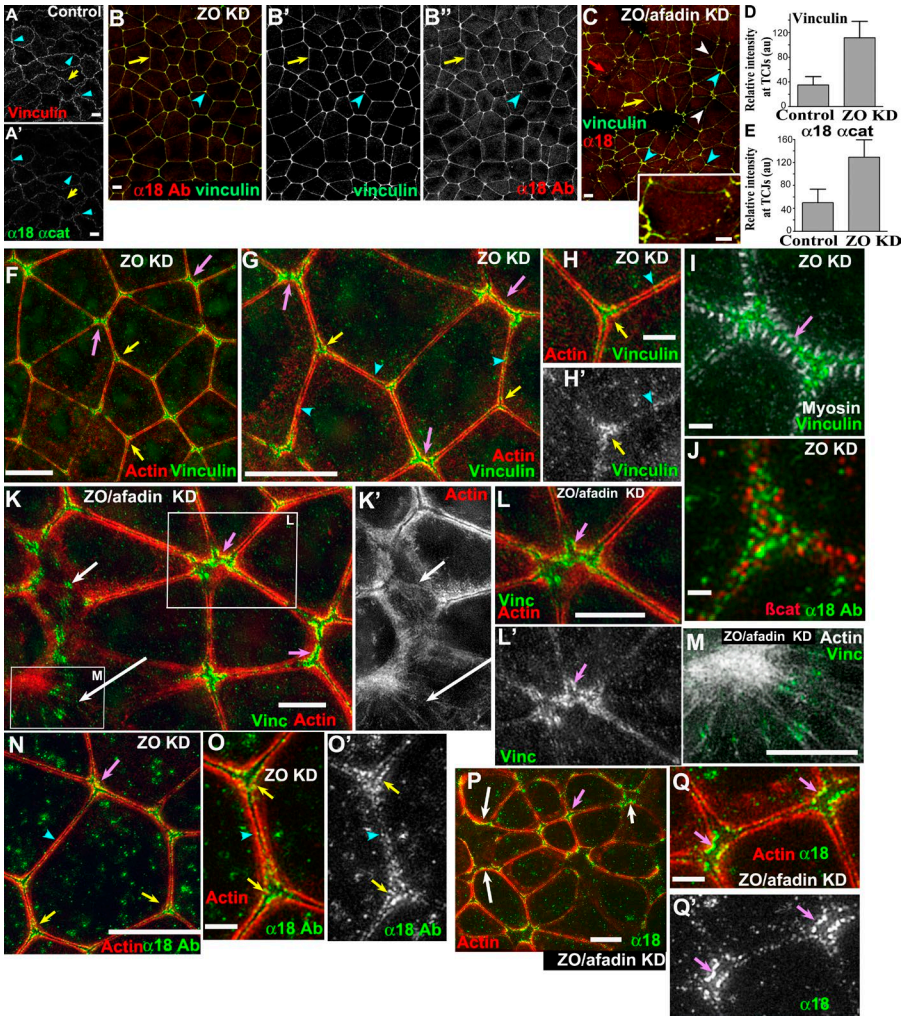

Figure 8. **Vinculin and α18 focus at tricellular and multicellular junctions in ZO KD.** (A–C and F–Q) 3-µm confocal (A–C) or 2-µm SIM (F–Q) apical projections. (B, D, and E) ZO KD. Vinculin and α18 are elevated at BCJs (A vs. B, arrows) and especially at TCJs (A vs. B [arrowheads]; D and E, mean line scan intensities). Error bars are SDs of >30 tricellular contacts (n = 3). au, arbitrary unit. (C) ZO/afadin KD. Vinculin and α18 are elevated but variable at TCJ/MCJs (arrowheads). At some BCJs, staining is fragmented (yellow vs. red arrows and inset). (F–J, N, and O) ZO KD. Vinculin and α18 enrichment at TCJs (yellow arrows) and MCJs (magenta arrows) is membrane proximal to actin (H and O) or myosin (I). (K–M, P, and Q) ZO/afadin KD. Vinculin and α18 line membrane-proximal edges of actin cables (L and Q, magenta arrows). In regions of ZA discontinuity (K and P, white arrows), they surround the region or align along actin filaments (M). Bars: (A–C, F, G, K–N, and P) 5 µm; (H–J, O, and Q) 1 µm.

minifilament orientation was unchanged (Fig. 6 M). Thus afadin is not essential to assemble the ZA actomyosin array after ZO KD or anchor it to BCJs.

Afadin KD in ZO KD cells had its greatest effects at TCJs/MCJs. SIM revealed that actomyosin organization was substantially altered at TCJs of ZO/afadin KD cells, spreading into a substantially broadened apical-basal region (Figs. 6 L, 7 E, and S4 [arrowheads]). Strikingly, the periodic linear myosin features extended along the membrane across the broadened F-actin network (Fig. 6, I and L [magenta arrows] and M). At moderately altered MCJs, Ecad remained strongly enriched (Fig. 7 D, arrowheads), Ecad puncta filled spaces between the broadened distributions of actin and myosin (Fig. 7 E, magenta arrows and inset), and EM continued to suggest that actin bundles terminate at a convoluted plasma membrane as electron-dense plaques (Fig. 6, N and N′). Intriguingly, these regions of expanded actin retained the ability to resist the apical rounding seen at the cell apices (Fig. S4, arrowheads). Thus ZO/afadin KD specifically altered actomyosin architecture at the ZA of TCJs, where our data suggest actin cables are anchored.

TCJs/MCJs are prominent sites of molecular-level tension

Our hypothesis that actin cables anchor end-on into the ZA at TCJs predicts that these contractile BCJ actomyosin cables would exert force on cadherin complexes there. The α-catenin epitope α18 and vinculin can serve as molecular measures of tension applied on proteins of the ZA (Yonemura et al., 2010). Control cells have weak, discontinuous vinculin and α18 colocalization at BCJs (Fig. 8, A and A′, yellow arrows; Bays et al., 2014), with little elevation at TCJs (Fig. 8, A and A′, arrowheads), consistent with a relatively relaxed actomyosin network. After ZO KD, α18 and vinculin increased at BCJs (Fig. 8, G and N, arrowheads; and Fig. S5, F and G) but were especially elevated at TCJs (Fig. 8, B, D–H, and N [yellow and magenta arrows]; and Fig. S5, D, E [yellow arrows], F, and G; overall α-catenin is not dramatically elevated [Fig. S5 H]), consistent with the idea that greater force may be applied to cadherin complexes there. It is important to note that vinculin and α18 enrichment was paralleled by increased Ecad, especially at TCJs (Fig. 7 C)—Ecad enrichment may thus contribute to increased α18 and vinculin recruitment. In fact, Ecad recruitment itself can be promoted by elevated contractility (Leerberg et al., 2014). Vinculin and α18 form punctate threads, which line scans revealed are membrane proximal to actin and myosin (Fig. 8, G and O, yellow arrows; Fig. S5, I–K; 18/21 borders analyzed) and interspersed with β-catenin puncta (Fig. 8 J), consistent with the idea that Ecad, the catenins, and vinculin help link actomyosin arrays to the membrane. This suggested that TCJs/MCJs might be sites where increased contractile force is applied to junctional proteins.

Strikingly, although vinculin and α18 accumulation at TCJs was relatively uniform after ZO KD (Fig. 8 B), their

distribution was much more heterogeneous after ZO/afadin KD (Fig. 8 C, blue vs. white arrowheads), even in places where the ZA was continuous. Vinculin and α18 were particularly elevated at short MCJs (Fig. 8 C, blue arrowheads), where SIM showed they decorated membrane-proximal borders of junctional F-actin (Fig. 8, K and L, P, and Q [magenta arrows]). There were also subtle changes along some BCJs of ZO/afadin KD cells, where α18 and vinculin became more punctate (Fig. 8 C, red vs. yellow arrows and inset). These differences paralleled cell border length—short, potentially hyperconstricted borders had high vinculin and α18 levels (Fig. 8 C, blue arrowheads), whereas longer, hyperrelaxed borders were depleted of them (Fig. 8 C, arrows and inset). This pattern correlated with the maintenance of high tension at short BCJs and somewhat lower tension at longer BCJs seen after laser cutting (Fig. 5 H). Overall, these data suggest that afadin affects cells' ability to distribute molecular-level force uniformly at TCJ/MCJs across a monolayer.

At the larger ZA discontinuities in ZO/afadin KD monolayers (Fig. 8, K and P, white arrows), SIM imaging showed a diffuse cortical actin filament network within them (Fig. 8 K′, white arrows). Ecad (Fig. 7, D [white arrow] and F), vinculin (Fig. 8, K [top white arrow] and M), and α18 (Fig. 8 P, white arrows) all decorated structures spanning or surrounding these regions. We consider in the Discussion how these larger discontinuities arise.

Sustained contractility exerted by neighbors is required for myosin but not afadin recruitment

The dramatic actomyosin arrays and balanced contractility of ZO KD cells were intriguing. In situations ranging from cytokinesis to apical constriction or convergent extension, actomyosin assembly is driven in part by positive feedback loops and can in turn be terminated by negative feedback (Surcel et al., 2010; Levayer and Lecuit, 2012). We thus explored whether internally generated signals downstream of ZO KD were sufficient for myosin recruitment or whether it was enhanced by feedback loops instigated by neighboring cells pulling on one another. To do so, we mixed ZO KD and control cells at different ratios, creating small islands of one cell type surrounded by the other (Fig. 9, B and C), reasoning that small islands of ZO KD cells surrounded by more compliant control cells would not experience the same forces exerted by their neighbors as when they were surrounded by more contractile ZO KD cells.

When small islands of control cells were surrounded by ZO KD cells, each retained the myosin distribution seen in uniform monolayers (Fig. 9 A): ZO KD cells had high cortical myosin whereas control cells had low levels (Fig. 9 D). Similarly, elevated afadin was seen only in ZO KD cells and not in small islands of control cells (Fig. 9 E), and vinculin localization was consistent with the idea that in this configuration, ZO KD cells exhibited high contractility and control cells lower contractility (Fig. 9 F). However, when small islands of ZO KD cells were surrounded by control cells, the result was quite different. ZA-associated myosin was markedly reduced in small islands of ZO KD cells, to levels comparable to surrounding control cells (Fig. 9 G), and cell shapes became less polygonal (Fig. 9 H). Thus full development of the ZA contractile array in a cell may depend on contractility of neighbors. In contrast, afadin was still recruited to the ZA in small islands of ZO KD cells (Fig. 9 H), but its distribution was more discontinuous (Fig. 9 H′) than in ZO KD cells (Fig. 9 A′). Thus afadin recruitment may be a more direct response to ZO KD, but its even distribution along the ZA may depend on signals arising from contractility of neighbors.

We next explored whether continuous myosin contractility is essential to maintain afadin at the ZA in response to ZO KD. Blebbistatin treatment of ZO KD cells to reduce myosin contractility dramatically fragmented the ZA actomyosin array (Fig. 9, I vs. J). Importantly, afadin still localized to the ZA, although, like actin and myosin, it became much more discontinuous (Fig. 9, I vs. J). ROCK inhibitors had a similar effect: afadin levels remained elevated but in a highly fragmented pattern (Fig. 9, K vs. L). This result suggests that myosin contractility is not essential for recruiting afadin to the ZA, but it is essential for maintaining the actomyosin array and afadin's uniform distribution along it.

Globally reducing Ecad-based adhesion has a phenotype distinct from afadin KD

Our data suggest that afadin KD in ZO KD cells does not generally decouple the actomyosin cytoskeleton from cell borders but instead specially affects TCJ/MCJs. To test whether globally reducing cadherin-based adhesion had a similar effect, we knocked down Ecad in the ZO KD background. We chose the clone with the largest Ecad reduction (~80% KD; Fig. S6 A) and examined its effect on cell shape, F-actin, and myosin. ZO/Ecad KD had major effects on cell shape and the cytoskeleton, but these were distinct from those resulting from ZO/afadin KD. ZO/Ecad KD led to two populations of cells differing in their degree of apical constriction (Fig. S6 B). The highly apically constricted cells retained a relatively isometric shape rather than taking on the elongated cell shapes seen after ZO/afadin KD (Fig. S6 B). The other cells had much larger apical areas and substantially reduced ZA actin and myosin (Fig. S6, C and D), but this reduction occurred all around the cell circumference. Thus, although globally reducing adhesion leads to different levels of contractility in different cells, it does not seem to be as unbalanced among different borders of the same cell. These data are consistent with the hypothesis that afadin KD does not act simply by globally reducing cell adhesion.

Afadin is a robust scaffold playing partially separable roles in cell shape and ZA integrity in response to elevated contractility

Afadin is a multidomain scaffolding protein (Fig. 10 A) that links junctional and cytoskeletal proteins. To help define its mechanism of action in response to elevated contractility, we asked which domains are essential for function. Afadin's N terminus has two Ras-association (RA) domains that bind the small GTPase Rap1 to activate afadin function. This is followed by Forkhead-associated and Dilute (DIL) domains, which thus far have only one binding partner, ADIP. The central PDZ domain binds the C termini of transmembrane Nectins, and, at least in *Drosophila*, Ecad. This is followed by a long, less-well-conserved linker with several proline-rich motifs binding partners such as ZO-1 and SHP-2, and a C-terminal F-actin binding domain.

We obtained a series of GFP-tagged afadin mutants, each deleting a different domain (Fig. 10 A; Nakata et al., 2007), and established several stable cell lines of each in the ZO/afadin KD background. All were expressed at least at the level of endogenous afadin (Fig. S7). We tested each for rescue of cell shape alterations and ZA discontinuities seen after ZO/afadin

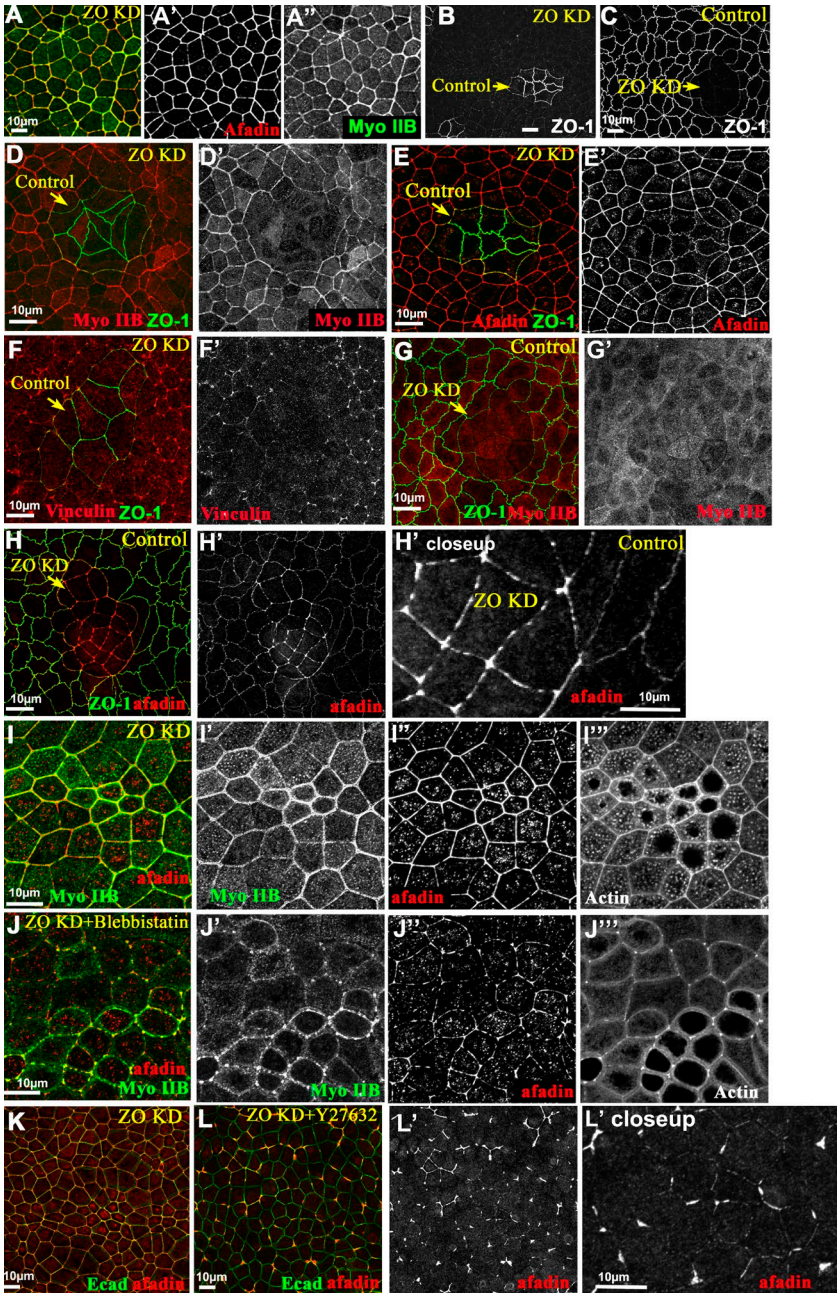

Figure 9. **Feedback from tissue-level contractility and myosin activity is required for myosin accumulation but not afadin recruitment.** Control, ZO KD, or mixed culture projections of apical 3-μm sections. Some cells treated with DMSO (control; A, I, and K); 0.1 mM blebbistatin (J); or 50 μM Y27632 (L). (B and D–F) Small islands of control cells in ZO KD monolayers. Each cell type retained patterns of myosin (D), afadin (E), and vinculin (F) seen in unmixed monolayers (e.g., A). (C, G, and H) Small islands of ZO KD cells in control cell monolayers. ZO KD cells had reduced cortical myosin (G), whereas afadin remained elevated cortically but became less continuous (A vs. H'). (I and J) Blebbistatin fragmented cortical myosin and afadin (I vs. J). (K and L) ROCK inhibition also made afadin more discontinuous.

KD, staining with the ZA marker Par3. To quantitatively assess rescue, we quantified differences in ZA integrity and cell shape between ZO and ZO/afadin KD cells as a baseline (Fig. 10, B vs. C; full data are in Tables S1, S2, and S3). Loss of ZA integrity manifested in two ways: smaller gaps in Par3 at TCJ/MCJs (less than the apical area of most cells; Fig. 10 C, red arrows) and larger ZA discontinuities extending several cell diameters (Fig. 10, C [green asterisks], L, and M; genotypes were scored blind). ZO KD cells had few small gaps (one/field of cells) and no large gaps, whereas ZO/afadin KD cells had many small (17/field) and large (17/field) gaps. We also quantified cell shape (Fig. 10 K). ZO KD cells are trapezoidal, with a mean major/minor axis ratio of 1.61. Many ZO/afadin KD cells are much more elongated (mean major/minor axis ratio of 2.31, with the distribution of major/minor axis ratios significantly broadened; Fig. S8 A). Finally, they differed in the number of neighbors surrounding each cell—although ZO KD cells had a sharp peak at six neighbors/cell, the distribution of neighbor numbers was significantly broader for ZO/afadin KD (Fig. S8 B1).

We then compared domain deletion mutants for rescuing ability. The results were quite striking, suggesting that afadin acts as a robust scaffold with different domains contributing to distinct aspects of its function. Full-length afadin (Fig. 10 D) fully rescued ZA integrity (one small and no large gaps/field; Fig. 10, L and M) and neighbor number (Fig. S8 B2) and largely restored cell shape symmetry (major/minor axis ratio 1.70; Fig. 10 K). AfadinΔDIL (Fig. 10 E) retained substantial function. It fully rescued ZA integrity (two small and no large gaps/field; Fig. 10, L and M) and neighbor number (Fig. S8 B3), although cell shape rescue was somewhat less robust (major/minor axis ratio 1.77; Figs. 10 K and S8 A). AfadinΔFAB (Fig. 10 F) also retained partial function, rescuing neighbor number (Fig. S8 B4) and cell shape (major/minor axis ratio 1.62; Figs. 10 K and S7 A). However, it did not fully restore

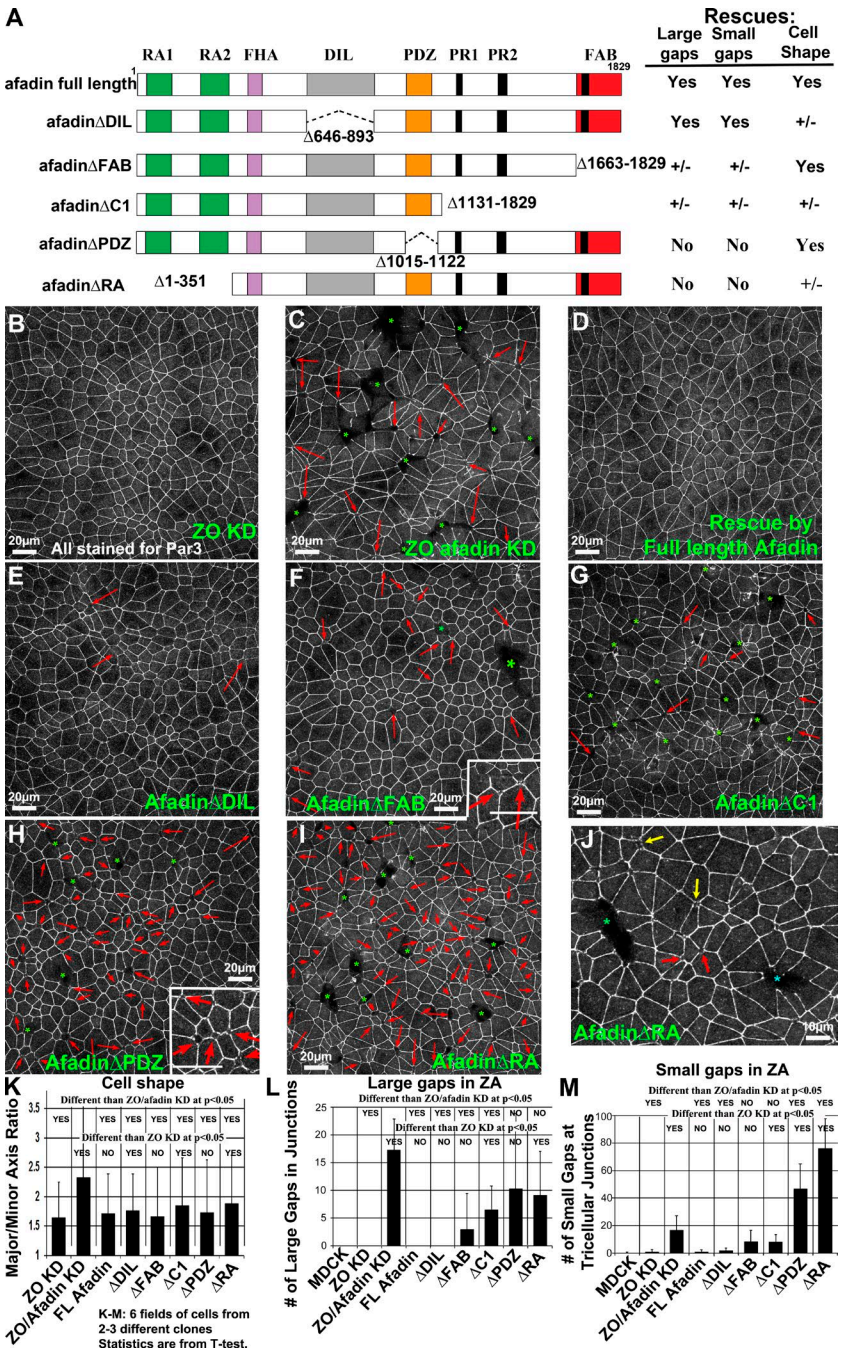

Figure 10. **Multiple afadin domains contribute differentially to different aspects of its function.** (A) Diagram of afadin and domain deletion mutants used. (right) Summary of their effectiveness at rescuing different aspects of afadin function. (B–I) Representative fields of ZO KD, ZO/afadin KD, or ZO/afadin KD cells rescued by indicated afadin mutants. Arrows, small gaps in ZA at TCJ/MCJs; asterisks, larger ZA gaps. Projections of apical 3-μm sections. (J) Closeup showing progressively larger gaps in ZA. (K) Quantification of major/minor axis aspect ratio. Error bars are SDs of >900 cells (n = 3). (L and M) Quantification of large (L) or small (M) ZA gaps. Error bars are SDs of each genotype.

ZA integrity, with significant numbers of both small (8.5/field) and large (three/field) gaps (Fig. 10, L and M). Many gaps were quite small, with Par3 disrupted right in the center of a TCJ (Fig. 10 F, inset). The larger C-terminal deletion, afadinΔC1 (Fig. 10 G), which removed the proline-rich linker, was even more debilitated. Although cell shapes and ZA integrity were qualitatively better than in ZO/afadin KD, afadinΔC1did not fully rescue neighbor number (Fig. S8 B5), cell shape (major/minor axis ratio 1.83; Figs. 10 K and S8 A), or ZA integrity (Fig. 10, L and M; 8.3 small gaps/field; 6.5 large gaps/field).

Deleting the PDZ or RA domains led to even more interesting phenotypes. Although afadinΔPDZ (Fig. 10 H) fully rescued cell shape (major/minor axis ratio 1.67; Figs. 10 K and S8 A) and neighbor number (Fig. S8 B6), it had a novel ZA integrity phenotype (Fig. 10 H). It provided little rescue of large gaps in the ZA (10 versus 13 after ZO/afadin KD; Fig. 10 L), although each gap was not as extensive. Strikingly, there were many more small gaps than in ZO/afadin KD cells (47 vs. 17; Fig. 10 M); most were small TCJ discontinuities (Fig. 10 H, inset). AfadinΔRA (Fig. 10 I) was the most impaired of the set. It only partially rescued cell shape and neighbor number (Fig. 10K; Fig. S8, A and B7). Further, afadinΔRA did not restore large gaps in the ZA (Fig. 10 L), and the number of small gaps was substantially elevated relative to ZO/afadin KD cells (76 versus 17; Fig. 10 M). Together, these data suggest distinct afadin roles in ZA integrity and cell shape, with different domain requirements. The novel phenotypes also provided insights into the nature of the ZA gaps in ZO/afadin KD cells. In domain deletion mutants, gaps varied in size from small gaps at individual TCJs (Fig. 10, F and H [insets] and J [yellow arrows]), to larger

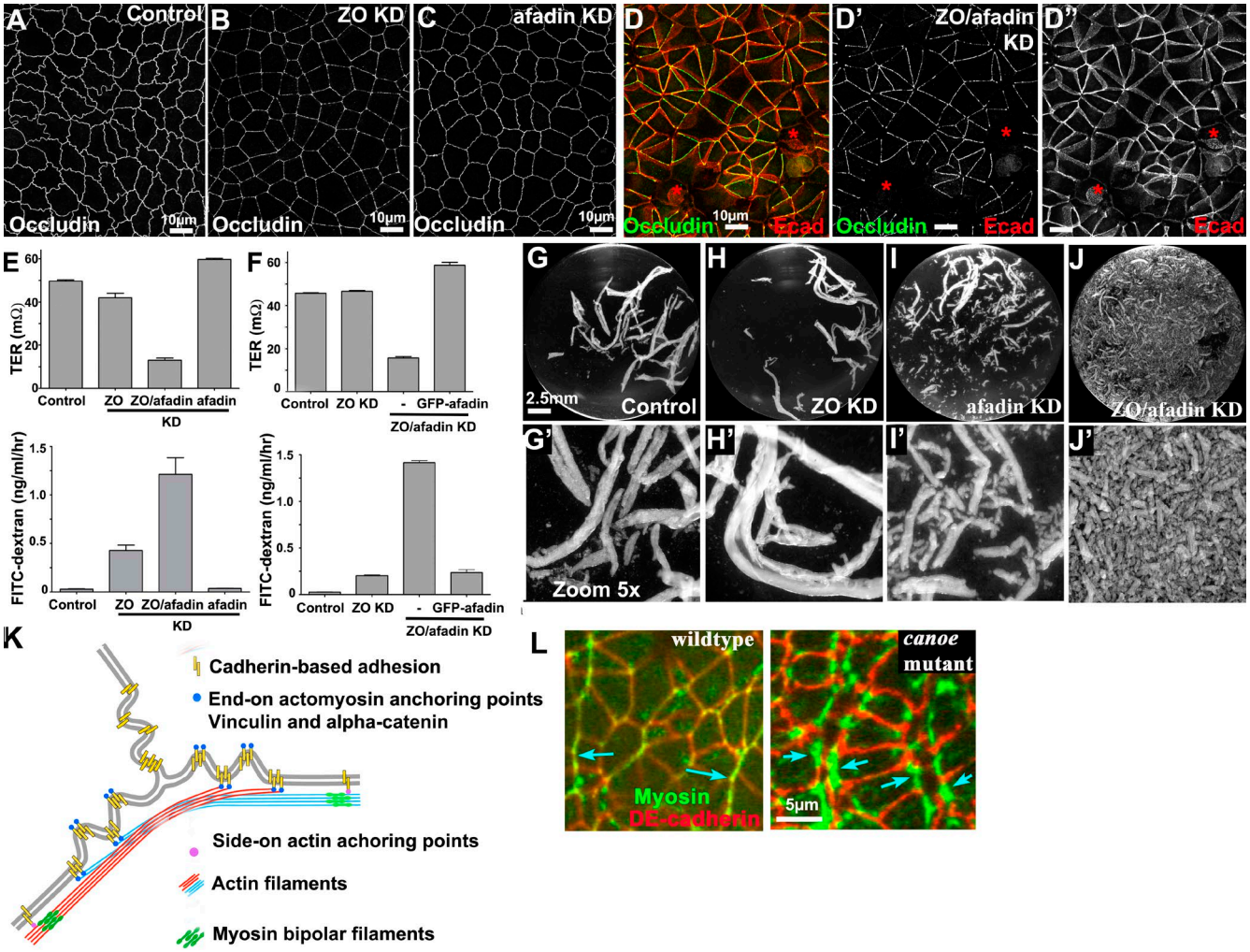

Figure 11. **ZO/afadin KD disrupts barrier function and resistance to external mechanical stress.** (A–D) Occludin and Ecad. Junctional occludin changes from continuous in control or afadin single KD to punctate after ZO KD. ZO/afadin KD dramatically disrupts junctional occludin. Ecad still localizes to regions where occludin is lost but no longer concentrates at ZA (D–D″, asterisks; projection, apical 6 µm). (E and F) Barrier function. TER (E) or dextran flux (F) across monolayer. ZO/afadin KD dramatically reduced barrier function, whereas afadin single KD had no effect. Error bars are SDs of three independent experiments. (G–J) Monolayers detached by dispase and mechanically disrupted by pipetting. (G′–J′) 5× zoomed images. ZO KD did not affect tissue integrity. Afadin single KD slightly reduced sheet integrity. ZO/afadin KD dramatically reduced this (I). (K) Model, ZA actomyosin organization in cells with increased contractility. Contractile actomyosin arrays run parallel to BCJs and make end-on contacts at TCJs, generating a "zig-zag" membrane topology at TCJs. (L) Germband extending wild-type or *canoe* mutant fly embryos—wild-type myosin localizes to planar polarized cables tightly localized to the ZA at anterior-posterior boundaries (arrows). Canoe loss results in myosin broadening.

gaps encompassing several TCJs (Fig. 10 J, red arrows), to large gaps at the center of cell rosettes (Fig. 10 J, blue asterisk). Perhaps these constitute a progression of successive ZA failure; in unrescued ZO/afadin KD cells, small gaps may open up further into large gaps, reducing small gap numbers and increasing large gap numbers. The initiating event (e.g., cell division or apical or basal extrusion) remains an open question.

ZO/afadin KD compromises the epithelial barrier

We next explored how altered ZA architecture affected tissue-level responses, hypothesizing that ZO/afadin KD might affect the epithelial barrier. ZO KD only subtly affected tight junction (TJ) structure and barrier function; TJ proteins such as occludin were reduced but remained distributed around the cell circumference (Fanning et al., 2012; Fig. 11, A vs. B), and steady-state transepithelial resistance (TER) was not altered, although the "leak" pathway for large uncharged solutes was increased (Fig. 11 E). Afadin single KD did not affect TJ protein localization or barrier function (Fig. 11, C and E). In contrast, ZO/afadin KD led to marked gaps in TJ proteins such as occludin (Fig. 11 D), claudin 2, and cingulin (not depicted) never observed in control, ZO KD, or afadin single KD cells. These gaps corresponded with discontinuities in apical Ecad (Fig. 11 D, asterisks). Strikingly, ZO/afadin KD dramatically decreased TER and increased 4-kD dextran flux >20-fold (Fig. 11 E). This was reversed by RNAi-resistant GFP-afadin (Fig. 11 F). Thus afadin acts directly or indirectly to maintain TJ function in response to increased contractility.

Afadin synergizes with ZO proteins to support epithelial resistance to external force

ZO/afadin KD did not disrupt epithelial sheet cohesion (Fig. 5 I) but did lead to dramatic cell shape defects in response to elevated ZA contractility. We next tested whether afadin KD altered responses to external mechanical stress, in which the orientation

of force vectors/stress tensors is distinct from those created by internal contractility. To do so, we detached cell sheets and mechanically disrupted them via manual pipetting (Sumigray et al., 2012). Control and ZO KD cell sheets were relatively resistant, with the sheet converted into large fragments (Fig. 11, G and H). In contrast, mechanically shearing afadin single KD cell sheets generated an increased number of small tissue fragments (Fig. 11 I), indicating that afadin has a role in tissue cohesion even in the absence of elevated contractility. However, this was subtle in contrast to the dramatic disruption of tissue cohesion in response to external stress seen in ZO/afadin KD cells (Fig. 11 J), suggesting synergy between ZO and afadin KD in disrupting tissue integrity under stress.

Discussion

Epithelia face twin challenges during development: to maintain epithelial integrity while undergoing dramatic cellular rearrangements. To accomplish this, cells rely on cell–cell junctions to maintain tissue integrity, but at the same time use these junctions as anchor points for the actomyosin cytoskeleton to generate force and drive cell shape change. One key issue is to determine the mechanisms by which cells carry out these seemingly conflicting tasks. We used the simplified MDCK model epithelium to explore this, combining genetic manipulation and superresolution microscopy to define the architecture underpinning cytoskeletal–junction connections, determine how contractility is balanced within cells and across the monolayer, and define a role for afadin in maintaining cell shape and tissue integrity in response.

ZO proteins inhibit ZA actomyosin assembly by inhibiting Shroom3 recruitment and thus ROCK activation

ZO KD has dramatic consequences in MDCK cells, substantially accentuating the apical ZA, with Ecad concentrated there rather than being almost uniform along the apical-basal axis, and with robust assembly of a contractile actomyosin network at the ZA. Our data help reveal the mechanism by which ZO proteins regulate ZA assembly. ZO KD leads to recruitment of Shroom3, a known contractility regulator, to the ZA. Our data suggest that Shroom3 then recruits ROCK, triggering ZA actomyosin assembly/activation. Intriguingly, recent work revealed a role for a Shroom/ROCK pathway in fly convergent extension (Simões et al., 2014), a process in which Canoe also plays an important role. Our data also help illustrate the diversity of pathways regulating ZA contractility in different species and tissue types. For example, mouse mammary cells use Willin and Par3 to cooperatively recruit aPKC to junctions, inhibiting contractility (Ishiuchi and Takeichi, 2011). In human colorectal cells, a Lulu2-p114RhoGEF pathway can stimulate apical contractility in a Shroom3 independent way (Nakajima and Tanoue, 2012), whereas NF2 KD reverts straight junctions to wavy cell borders (Chiasson-MacKenzie et al., 2015).

New insights into the structural basis of bicellular borders as units of contractility

Cell shape change is driven by actomyosin contractility coupled to cell junctions (Levayer and Lecuit, 2012). The original textbook view of the ZA as a circumferential cadherin ring linked to an underlying actin ring has been significantly refined by new experiments and modeling. For example, fly and worm apical constriction is driven by a contractile actomyosin network that spans the apical surface and makes orthogonal contacts with the ZA (Martin et al., 2009; Roh-Johnson et al., 2012). In contrast, in fly convergent extension or dorsal closure, the network and thus contractility is planar polarized to anterior-posterior borders or the leading edge. However, in all, contractility can occur independently on individual bicellular borders between pairs of TCJs. Similarly, modelers developed vertex models, providing a theoretical underpinning (Fletcher et al., 2014).

Our superresolution and EM images provide novel molecular insights into how the ZA is remodeled in response to elevated contractility. Bundled actin filaments run parallel to the membrane along BCJs, linked in a sidelong fashion to punctate cadherin complexes. Individual BCJs contract and relax independently of other borders in the same cell, defining a contractile unit bounded by TCJs. At TCJs, actomyosin arrays of adjacent cells splay out and Ecad accumulates at elevated levels in the membrane proximal space. Our EM images suggest that the arrays do not detach from membrane, but instead actin bundles along one BCJ separate into fan-like arrays and anchor end-on at discrete puncta just past the TCJ (Fig. 11 K). Consistent with this, vinculin and the α18 epitope, which can reflect force exerted on junctional complexes, are enhanced in puncta flanking TCJs that we predict are membrane attachment sites for the ZA array. The parallels with morphogenetic movements (Kiehart et al., 2000; Bertet et al., 2004; Fernandez-Gonzalez et al., 2009; Martin et al., 2010) are intriguing, suggesting that similar molecular architectures may be at play. Superresolution imaging of the ZA during these dynamic events will help resolve this.

Feedback loops during the ZA response to contractility

Cadherin complexes and junctional actomyosin are reciprocally reinforcing, via positive and negative feedback loops. Sensors within the ZA allow cytoskeletal force to be sensed, helping initiate feedback. Recent work has begun to illuminate this, revealing, e.g., a pathway by which contractility stimulates Ena/VASP-driven actin assembly at the ZA, in turn promoting Ecad recruitment (Leerberg et al., 2014). We observed similar interplay. Increased contractility stimulated by ZO KD is coupled with strong apical Ecad enrichment, forming a prominent ZA not present in control cells. In the *X–Y* plane, Ecad is especially elevated at TCJs and MCJs. This is consistent with a hypothesis that elevated contractility stimulates Ecad recruitment. It will be exciting to define underlying mechanisms. There also may be feedback loops within the actomyosin cables. Myosin assembly and contractility can be regulated in a cyclical fashion, with periodic contraction and relaxation cycles (Munro et al., 2004; Martin et al., 2009; Solon et al., 2009; Roh-Johnson et al., 2012). The molecular basis remains unclear, but increased contractility may trigger increased myosin recruitment. Similar feedback may help explain our data. ZO KD leads to assembly of a robust ZA actomyosin machine, which undergoes cycles of contraction and relaxation. However, small islands of ZO KD cells in monolayers of less contractile control cells did not establish the same robust myosin network. Perhaps initial actomyosin assembly drives some contractility, which, as cells pull on adjacent neighbors, engages a positive feedback loop, leading to the robust actomyosin array seen at steady state. It will be interesting to define mechanisms underlying this, including sensors required and mechanisms to engage and then inactivate

feedback at different tension thresholds to maintain homeostasis. Investigating the dynamic localization of junctional and cytoskeletal proteins will also be useful.

Afadin maintains ZA integrity at TCJs in response to elevated contractility

ZO/afadin KD cells provided a relatively simple system in which to explore afadin's mechanism of action. *Drosophila* Canoe loss impairs apical constriction and germband elongation by altering the relationship between the ZA and the actomyosin network. We thus proposed that Canoe/afadin is a junction/actin cross-linker. Our new data suggest this is only part of the story. We first ruled out several potential mechanistic roles. Afadin KD in ZO KD cells did not impair robust ZA actomyosin assembly or its anchoring laterally along BCJs, ruling out two mechanisms of action. Further, ZA actomyosin contractility remained intact.

Instead, our data suggest that afadin's role is most important at TCJ/MCJs, where our data suggest contractile force on cadherin complexes may be highest. After ZO/afadin KD, the focused apical actomyosin cables at the ZA broadened at TCJs to a less focused actin network, spreading along the apical-basal axis. Myosin minifilament assemblies lengthened to span this broadened network. Simultaneously, Ecad puncta spread over a broader zone in the *X–Y* axis. Interestingly, this echoes the myosin expansion after Canoe loss during fly germband extension, from tight membrane-bound cables to a broader distribution (Fig. 11 L). Thus afadin is essential to maintain the ZA at TCJs, with its tight apical focusing of actomyosin in response to elevated contractility. Our afadin domain deletion mutants, which provide an allelic series of less severe defects, offer further insights into afadin's mechanistic roles. They reveal two partially independent roles. Some mutants fail to rescue the cell elongation of ZO/afadin KD cells. Others have more subtle defects at TCJs, suggesting a possible sequence of events leading to the larger-scale defects in ZA continuity seen after ZO/afadin KD. One can imagine how small openings at individual TCJs seen in these mutants could, if they occurred at adjacent TCJs, lead to larger-scale failures, gradually expanding to form the large ZA gaps seen in the ZO/afadin KD monolayer. Intriguingly, these larger-scale defects occur at the center of cell rosettes, where a series of short BCJs are adjacent—these are the borders where our laser ablation suggests high tension is maintained. We do not think this role involves the TCJ protein tricellulin (Furuse et al., 2014), as its localization is not altered after ZO KD (Fanning et al., 2012) and tricellulin KD did not disrupt the actomyosin cytoskeleton assembled after ZO KD (unpublished data).

What molecular role might afadin play? Intriguingly, in many cell types, afadin is largely restricted to the ZA, unlike cadherin, which localizes all along the lateral membrane. In our minds, the most likely possibility is that afadin helps cross-link actin and junctional proteins and focus them apically, preventing the spreading seen after ZO/afadin KD. For example, afadin's known interactions with tight junction proteins may be important (Ooshio et al., 2010; Monteiro et al., 2013). In this model, afadin would be most critical at TCJs, where we hypothesize contractile filaments anchor end-on into junctions, focusing force on cadherin complexes. Our domain deletion data further suggest that afadin acts as a robust scaffolding protein, interacting in a multivalent way with diverse partners, as no individual domain deletions completely abrogate function. Interactions mediated by the RA domain, likely with Rap1, and those of the PDZ domain, perhaps with nectins (Takai et al., 2008) or cadherins (Sawyer et al., 2009), are particularly important. However, this model by itself does not fully explain the phenotype observed, as afadin is also required to maintain a balance of border lengths. In its absence, some bicellular borders become hyperconstricted and others hyperextended—this requires a distinct but overlapping set of afadin domains. It will be important to test different proposed mechanisms and the afadin-binding partners involved and combine developing predictive physical theories with experimentation, to bridge the gap between molecular interactions and forces at the cell and tissue level.

Materials and methods

Reagents and antibodies

All reagents used in this study were from Sigma-Aldrich unless otherwise indicated. The antibodies and concentrations used for immunocytochemistry (ICC) and Western blotting (WB) are as follows: mouse anti–ZO-1 (1:100 ICC, 1:300 WB), rabbit anti–ZO-1 (1:500 ICC), rabbit anti–ZO-2 (1:100 ICC, 1:500 WB), rabbit anti–ZO-3 (1:100 ICC, 1:250 WB), rabbit anti–αE catenin (1:200 ICC, 1:500 WB), mouse anti-occludin (1:300 ICC, 1:1,000 WB), and mouse anti–claudin 2 (1:100 ICC, 1:500 WB): Life Technologies; rat anti–ZO-1 clone R40.76 (1:25 ICC, 1:100 WB): Anderson et al. (1988); rabbit anti–myosin IIA and rabbit anti–myosin IIB (1:250 ICC, 1:1,000 WB): Covance Research Products; rabbit anti–α-actinin 4 (1:100 ICC): GeneTex; rabbit anti–β catenin (1:5,000 ICC, 1:2,000 WB), mouse anti-vinculin (1:100 ICC, 1:500 WB), rat anti-Ecad (1:500 ICC), rabbit anti-afadin (1:500 ICC), and rabbit anti-VASP (1:1,000 WB): Sigma-Aldrich; mouse anti-AF6/afadin (1:100 ICC, 1:1,000 WB), mouse anti-aPKCλ (1:250 ICC), and mouse anti-VASP (1:125 ICC): BD Biosciences; rabbit anti-PAR3 (1:100 ICC, 1:250 WB), mouse anti–α actin (1:1,000 WB), and rabbit anti-p34 (1:250 ICC): EMD Millipore; goat anti-aPKCζ (1:200 ICC, 1:200 WB) and goat anti-ROCK1 (1:50 ICC): Santa Cruz Biotechnology; mouse anti–phospho-myosin light chain (1:100 ICC): Cell Signaling Technology; rabbit anti-Shroom2 (1:100 ICC) and rabbit anti-Shroom3 (1:100 ICC): Jeffrey Hildebrand, University of Pittsburgh, Pittsburgh, PA; guinea pig anti-tricellulin (1:100 ICC): Fanning et al. (2012); rat anti–αE catenin (1:200 ICC): Yonemura et al. (2010); mouse anti-gp135 (1:100 ICC): Ojakian and Schwimmer (1988); and rabbit anti-cingulin (1:500 ICC, 1:2,500 WB): Cordenonsi et al. (1999).

Stable or transient knockdown of afadin or Shroom3 using pSUPER/shRNA constructs or stealth siRNAs

Afadin expression in MDCK II Tet-Off cells (clone T23; Takara Bio Inc.) was targeted for KD using two different sets of shRNA expression vectors. Both sets had an identical effect on ZA structure and cell morphology. Set A targeted sequences were 5′-GCATGGATGCTGAGACTTA-3′ and 5′-GACAATCJCTGCTGTCJTACC-3′ and were designed using an online algorithm (GE Healthcare). Set B was provided by M. Caplan (Yale University, New Haven, CT) and targeted sequences were 5′-GAAATATGGTCJTAGAGAAA-3′ and 5′-GGGAGAAGCTAGAGAAGCA-3′ (Zhang et al., 2011). Forward and reverse oligonucleotides were synthesized (Thermo Fisher Scientific), annealed, and cloned into pSUPER.basic plasmid (Oligoengine) per the manufacturer's instructions. Shroom3 expression was transiently depleted by Stealth siRNAs (Life Technologies); Shroom3-1, 5′-CCCUAGAGCCUCAGCAGCAAGUUAA-3′; Shroom3-2, 5′-CAGAAGACCUCAGAAGACAUCAGAA-3′ (Nakajima and Tanoue, 2010). Stealth RNAi negative control (Life Technologies) was used for control RNAi. Transfection of Stealth siRNA was performed using RNAi MAX reagent (Life Technologies).

Cell culture and transfection

MDCK II Tet-Off cells were cultured in high-glucose DMEM supplemented with 10% FBS, penicillin, and streptomycin (standard media) on Transwell-Clear filter inserts (Corning) or acid-washed glass coverslips unless otherwise noted. To generate stable cell lines, plasmid DNAs were introduced into MDCK, ZO-1 KD (KD#1, clone 4A6; Van Itallie et al., 2009), or ZO-1/ZO-2 double-KD (ZO KD, clone 3B3; Fanning et al., 2012) cells using the Amaxa Nucleofector kit L (Lonza) according to the manufacturer's instructions with program L-005, 2×10^6 cells, and 5.0 µg DNA (total). Plasmids for drug selection, where necessary, were included at 20-fold dilution relative to the shRNA vectors. To generate afadin KD lines, the pSUPER shRNA plasmids were cotransfected with pBlast49 (InvivoGen) or pTK-HYG (Clontech) and selected in standard media containing 10 µg/ml Blasticidin (InvivoGen; MDCK and ZO-1 KD cells) or 200 µg/ml Hygromycin B (ZO KD cells), respectively. Drug-resistant clones were isolated using cloning rings and tested for knockdown efficacy by Western blotting and immunocytochemistry. Western blotting techniques are outlined in Fanning et al. (2012). To quantify the levels of knockdown, densitometry for the Western blot bands was performed using Image Studio software (Li-COR). The levels of afadin were reduced to ∼5% in the single KD (afadin KD) and 10% in the triple KD (ZO/afadin KD).

To construct stable cell lines expressing MRLC-GFP or GFP-afadin, or ZO or ZO/afadin (clone 1A1) KD cells were cotransfected with pLL7-MRLC-GFP (J. Bear, University of North Carolina at Chapel Hill, Chapel Hill, NC), pEGFP-rat afadin full length (aa 1–1,829; Hoshino et al., 2005), or different domain-deleted afadin mutants (Nakata et al., 2007) and the pSV2-HisD plasmid encoding the selectable marker histidinol acetyltransferase. Stable clones were isolated using cloning rings after selection for 10–12 d in standard media supplemented with 6.0 mM histidinol (Hartman and Mulligan, 1988).

Immunocytochemistry

Cells were cultured for at least 7 d in Transwell-Clear filter inserts or on acid-washed glass coverslips before drug treatment or fixation. Cells were washed twice with RT PBS supplemented with 1.8 mM $CaCl_2$ and fixed in either ice-cold ethanol for 30 min or buffered 1% formaldehyde (PBS or 0.1 M Hepes, pH 7.4) for 20 min. Formaldehyde-fixed cells were permeabilized by 0.2% Triton X-100 or 0.02% saponin in PBS with 30 mM glycine for 10 min. Washed filter inserts were excised with a razor blade and transferred to a 12-well plate. Cells were blocked in 5% normal donkey serum in PBS or PBS with 0.02% saponin. All primary and secondary antibodies were diluted in PBS containing 1% IgG/protease-free BSA in PBS or PBS with 0.02% saponin. Filters and coverslips were inverted onto a 50-µl drop of diluted antibodies. Primary antibodies were incubated overnight at 4°C, and secondary antibodies were conjugated with Alexa dyes (Life Technologies) or Cy dyes (Jackson ImmunoResearch Laboratories, Inc.) for 1 h at RT in a humidified container. Washed samples were mounted on a microscope slide using 10% (wt/vol) Mowiol 4-88 (Calbiochem) with 1% *n*-propylgallate, AquaPolymount (Polysciences), or Vectashield H-1000 (Vectorlabs), as indicated in the figure legends.

For the contractility feedback experiments, cells were cocultured at different seeding ratios (for small control islands, MDCK/ZO KD 1:10; for small ZO KD islands, MDCK/ZO KD 5:1) for at least 7 d before fixation.

For the absolute measurement and comparison of ZA protein intensities, control and ZO KD cells were cocultured at 1:10 and stained for α18, α-catenin, vinculin, and Ecad. The apical 3-µm section was imaged and processed for *z* projection. Line scan analysis was done across the BCJ or at the TCJ using ImageJ (line width 10 pixels). The cytosolic background was very low and similar to control and ZO KD cells. The intensities at the ZA were graphed and aligned for comparison without normalization.

Light and electron microscopy

For confocal microscopy, samples were imaged using the LSM 710 Duo (ZEISS) with a 63× objective (1.4 NA; ZEISS). Images were acquired at 1,024 × 1,024 resolution, with 0.3-µm spacing along the *z*-axis. Image acquisition and initial processing was done using ZEN2009 software (ZEISS). Unless otherwise noted, images are maximum-intensity projections of 3-µm-thick slices. Image scaling (contrast and gamma intensity) was conserved between different panels from the same experiment.

For SIM, cells were grown on acid-washed glass coverslips and mounted on glass slides with Vectashield H-1000. Images were acquired using DeltaVision OMX Imaging System (GE Healthcare) with *x-y-z* dimensions of 0.08 × 0.08 × 0.125 µm and a 60× 1.42 NA oil immersion objective. Reconstruction from SI images and axial alignment were done using softWoRx software (GE Healthcare). For live-imaging of cells expressing MRLC-GFP, cells were grown on 35-mm glass-bottom dishes (MatTek Co.) in standard medium, which was replaced with OptiMEM (Life Technologies) 60 min before imaging. Images were acquired every 2 or 5 min using a FV1000 MPE laser confocal microscope (Olympus) with a PlanApo 60× 1.42 NA oil immersion objective. Cell fixation, sectioning, and staining for electron microscopy were performed as previously described (Fanning et al., 2012).

Image processing

Heat maps were generated using a spectrum view option in ZEN 2009 image software (ZEISS). The display option for individual channels was changed from grayscale to spectrum view, and the contrast was adjusted to set the maximum pixel value. The adjusted images were exported as TIFF files using full-resolution image window mode. Line scan analysis was performed using ImageJ plot histogram option. Line width was set at either 10 or 50 pixels, depending on the image resolution, to encompass the junctional staining. The intensity across the line was plotted as a histogram using the plot histogram function, and the values per individual pixel were exported to an Excel file using the copy option. Peak positions were aligned based on the maximum peak value along the line, and the mean and SD were calculated. Graphs were generated using GraphPad Prism 4 (GraphPad Software). 3D reconstruction was done using Volocity volume-rendering software (Perkin Elmer). The stack images were imported, and the brightness and contrast were adjusted. 3D rotation and isosurface rendering were done using 3D opacity mode. The adjusted images were exported as TIFF files. Analysis of cell shape descriptors including major/minor axis aspect ratio was performed by calculating the major and minor axis aspect ratios of individual cell outlines from segmented Par3 staining using the particle analysis function in ImageJ. The different steps of processing involved the detection of cell contours that were edited semimanually using image thresholding. Neighbor number was calculated from the segmented images by Delaunay triangulation algorithm using Delaunay Voronoi function in ImageJ. In assembling figures, Adobe Photoshop 7.0 was used to adjust input levels to span the entire output grayscale and adjust brightness and contrast. When protein levels were compared, images were equally adjusted.

Analysis of cell motility

The velocity fields were obtained using PIV technics on MATLAB (The MathWorks) and MatPIV v. 1.6.1 (GNU public license software [Sveen, 2004]). Images were divided into interrogation windows of 24 pixels (∼20 µm). The cross-correlation of interrogation windows from two consecutive images gave a displacement value and thus

the velocity. Interrogation windows overlapped each other by 75%, as there is a velocity vector every 6 pixels. A global filter and a local filter were applied. Spurious vectors were replaced by interpolation of neighboring vectors.

We calculated the spatial correlation function $C(r)$ of the velocity field for every time point using the following formula: $C(r) = [v(r') \cdot v(r' + r)]_{r'}/\{[v(r')^2]_{r'} \cdot [v(r' + r)^2]_{r'}\}^{1/2}$, where v refers to the two component velocity vectors (v_x, v_y) from the PIV minus the mean velocity of the field of view; r and r′ are vectors of coordinate; r is the norm of the vector r; and $<\ldots>_{r'}$ is the mean over every position vector r′. The correlation function indicates how much in mean cells at a given distance r are moving in a coordinated manner. The spatial correlation length is obtained when the correlation function first crosses zero.

The divergence of the velocity field,

$$\nabla \cdot v = \frac{\partial v_x}{\partial x} + \frac{\partial v_y}{\partial f},$$

was computed using a homemade algorithm adapted from the method described in Zehnder et al. (2015). Based on this method, we calculated the divergence at a given point with the integration of the normal component of the velocity vectors included in a ring centered on this point. The obtained value is then normalized by the area within the ring. The value of the ring radius has to be chosen and should be larger than a few cells but smaller than the large-scale observed patterns. We used a radius of ∼32 µm (40 pixels). The sign of the divergence gives an indication of whether the tissue is contracting (negative value, blue, inward movement) or expanding (positive value, red, outward movement). From the spatial correlation function of the divergence field, we inferred the interdistance between the contracting and expanding patches of cells.

Laser ablation of cell–cell contacts

Junctional recoil after laser ablation was measured as previously described (Leerberg et al., 2014). In brief, a constant region of interest with the longer axis orthogonal to Ecad-GFP–labeled cell–cell contacts was irradiated with a Ti:sapphire laser (Chameleon Ultra, Coherent Scientific) tuned to 790 nm (26 iterations, 26% transmission) mounted on a confocal microscope (LSM510 meta; ZEISS) with a 37°C heating stage. Images (256 × 256 pixels, 0.14 µm/pixel) were acquired with a 63× (1.4 NA) oil Plan Apochromat immersion lens at 2× digital zoom. Time-lapse images were acquired four frames after ablation with an interval of 4.8 s per frame. The distance between vertices of ablated contacts was measured using MtrackJ plugin (ImageJ), as a function of time. Data were averaged from a minimum of 30 contacts from three independent experiments. Image analysis was done as described previously (Leerberg et al., 2014). Statistical analysis for initial recoil velocities was performed by nonparametric *t* test, as indicated in the corresponding figure legends.

Epithelial sheet integrity assay and barrier function

Cells were grown in six-well plates for 7 d, washed twice with HBSS, and incubated with a 1:1 mixture of dispase solution (BD Biosciences) in HBSS for 2 h at 37°C. When the cells lifted off of the dish in a confluent sheet, they were subjected to mechanical disruption by pipetting up and down with a P1000 pipet 10 times. The cell sheet or cell sheet fragments were imaged using a smartphone camera or Leica dissecting microscope. The measurement of TER (Colegio et al., 2002) and fluorescein-dextran flux across monolayers has been described (Van Itallie et al., 2009). All physiologic measurements of cell lines derived for this article were performed in triplicate on three distinct clonal isolates.

Online supplemental material

Fig. S1 shows that the levels of adherens junctions, TJ, polarity proteins, and actomyosin regulators were not affected by knockdown of afadin, and that GFP-afadin rescues the actomyosin phenotype and barrier defects of ZO/afadin KD cells. Fig. S2 shows that ROCK activity is required for myosin recruitment at the ZA in response to the elevated contractility. Fig. S3 provides montages of live imaging showing that ZO/afadin KD cells remain dynamically contractile and exhibit dramatic cell shape changes. Fig. S4 shows the 3D architecture of ZO/afadin KD cells and confirms that despite apical gaps in the ZA, they maintain intact basolateral contacts and stress fibers. Fig. S5 shows the levels of Ecad, α18, and vinculin increase at bicellular contacts and tricellular junctions in ZO KD cells. Fig. S6 shows that Ecad KD disrupts the uniform distribution of actomyosin array and cell shape in ZO KD. Fig. S7 shows the expression levels of afadin with domain deletions. Fig. S8 shows the comparison of the distribution of major/minor axis ratio and neighbor numbers in afadin rescue clones with different domains deleted. Videos 2, 3, and 4 show full-field (Videos 2 and 4) and closeup (Video 3) versions of bright field time-lapse imaging of MDCK, ZO KD, and ZO/afadin KD. Videos 1 and 5 show full fields of fluorescent time-lapse imaging of ZO KD and ZO/afadin KD cells expressing MRLC-GFP. Videos 6 and 7 show MRLC-GFP–expressing ZO/afadin KD cells undergoing dynamic cell shape changes and restoring epithelial architecture at the ZA level. Table S1 shows the mean and SD of the major/minor axis ratio, the number of large gaps and small gaps, and the p-values from the *t* test between rescue lines and ZO KD or ZO/afadin KD. Table S2 shows the p-values from χ^2 of independence to compare the distribution of the major/minor axis ratio and the number of neighbors. Table S3 shows the raw data that were binned to analyze the distribution of the aspect ratio and the number of neighbors. Online supplemental material is available at http://www.jcb.org/cgi/content/full/jcb.201506115/DC1.

Acknowledgments

We thank John Poulton for advice and assistance with statistics; Teresa Bonello, Lathiena Manning, Daniel Dickinson, Scott Williams, Kaelyn Sumigray, Amy Maddox, Peifer laboratory members, and the anonymous reviewers for thoughtful conversations and comments on the manuscript; Yoshimi Takai, Michael Caplan, Ian Macara, Richard Mulligan, Masatoshi Takeichi, James Nelson, Jim Bear, Sandra Citi, Klaus Ebnet, and David Courson for reagents; Richard Cheney for scientific support; Susan Whitfield for artistry in Fig. 11 K; Patrina Pellett and Tony Kriepe for help with the Deltavision OMX imaging; and our collaborators from University of North Carolina Chapel Hill microscope facilities, Victoria Madden, Michael Chua, and Neal Kramarcy.

This work was supported by National Institutes of Health grant R01GM47957 to M. Peifer, National Institutes of Health grant R01DK061397 to A.S. Fanning and James Anderson, the Human Frontier Science Program and the National Health and Medical Research Council of Australia (1037320 and 1044041) to A.S. Yap, and the European Research Council under the European Union's Seventh Framework Program (FP7/2007-2013)/European Research Council grant agreement 617233 and the LABEX "Who Am I?" to R.-M. Mège and B. Ladoux.

The authors declare no competing financial interests.

Author contributions: W. Choi, A.S. Fanning, and M. Peifer conceived the study. B.R. Acharya and A.S. Yap designed, carried out, and analyzed the laser cutting to measure border tension. M.-A. Fardin, B. Ladoux, R.-M. Mège, and G. Peyret analyzed cell velocities and divergence and segmented images, calculated major/minor axis

aspect ratios, and analyzed neighbor number. M. Peifer analyzed cell border fluctuations and ZA discontinuities and aided with neighbor number analysis, and A.S. Fanning carried out EM and assessed barrier function. All other experiments were carried out by W. Choi. W. Choi, A.S. Fanning, A.S. Yap, and M. Peifer wrote the manuscript with input from the other authors.

Submitted: 23 June 2015
Accepted: 21 March 2016

References

Anderson, J.M., B.R. Stevenson, L.A. Jesaitis, D.A. Goodenough, and M.S. Mooseker. 1988. Characterization of ZO-1, a protein component of the tight junction from mouse liver and Madin-Darby canine kidney cells. *J. Cell Biol.* 106:1141–1149. http://dx.doi.org/10.1083/jcb.106.4.1141

Bays, J.L., X. Peng, C.E. Tolbert, C. Guilluy, A.E. Angell, Y. Pan, R. Superfine, K. Burridge, and K.A. DeMali. 2014. Vinculin phosphorylation differentially regulates mechanotransduction at cell-cell and cell-matrix adhesions. *J. Cell Biol.* 205:251–263. http://dx.doi.org/10.1083/jcb.201309092

Bertet, C., L. Sulak, and T. Lecuit. 2004. Myosin-dependent junction remodelling controls planar cell intercalation and axis elongation. *Nature.* 429:667–671. http://dx.doi.org/10.1038/nature02590

Blankenship, J.T., S.T. Backovic, J.S. Sanny, O. Weitz, and J.A. Zallen. 2006. Multicellular rosette formation links planar cell polarity to tissue morphogenesis. *Dev. Cell.* 11:459–470. http://dx.doi.org/10.1016/j.devcel.2006.09.007

Chiasson-MacKenzie, C., Z.S. Morris, Q. Baca, B. Morris, J.K. Coker, R. Mirchev, A.E. Jensen, T. Carey, S.L. Stott, D.E. Golan, and A.I. McClatchey. 2015. NF2/Merlin mediates contact-dependent inhibition of EGFR mobility and internalization via cortical actomyosin. *J. Cell Biol.* 211:391–405. http://dx.doi.org/10.1083/jcb.201503081

Choi, W., K.C. Jung, K.S. Nelson, M.A. Bhat, G.J. Beitel, M. Peifer, and A.S. Fanning. 2011. The single *Drosophila* ZO-1 protein Polychaetoid regulates embryonic morphogenesis in coordination with Canoe/afadin and Enabled. *Mol. Biol. Cell.* 22:2010–2030. http://dx.doi.org/10.1091/mbc.E10-12-1014

Colegio, O.R., C.M. Van Itallie, H.J. McCrea, C. Rahner, and J.M. Anderson. 2002. Claudins create charge-selective channels in the paracellular pathway between epithelial cells. *Am. J. Physiol. Cell Physiol.* 283:C142–C147. http://dx.doi.org/10.1152/ajpcell.00038.2002

Cordenonsi, M., F. D'Atri, E. Hammar, D.A. Parry, J. Kendrick-Jones, D. Shore, and S. Citi. 1999. Cingulin contains globular and coiled-coil domains and interacts with ZO-1, ZO-2, ZO-3, and myosin. *J. Cell Biol.* 147:1569–1582. http://dx.doi.org/10.1083/jcb.147.7.1569

Ebrahim, S., T. Fujita, B.A. Millis, E. Kozin, X. Ma, S. Kawamoto, M.A. Baird, M. Davidson, S. Yonemura, Y. Hisa, et al. 2013. NMII forms a contractile transcellular sarcomeric network to regulate apical cell junctions and tissue geometry. *Curr. Biol.* 23:731–736. http://dx.doi.org/10.1016/j.cub.2013.03.039

Fanning, A.S., C.M. Van Itallie, and J.M. Anderson. 2012. Zonula occludens-1 and -2 regulate apical cell structure and the zonula adherens cytoskeleton in polarized epithelia. *Mol. Biol. Cell.* 23:577–590. http://dx.doi.org/10.1091/mbc.E11-09-0791

Fernandez-Gonzalez, R., S.M. Simoes, J.C. Röper, S. Eaton, and J.A. Zallen. 2009. Myosin II dynamics are regulated by tension in intercalating cells. *Dev. Cell.* 17:736–743. http://dx.doi.org/10.1016/j.devcel.2009.09.003

Fletcher, A.G., M. Osterfield, R.E. Baker, and S.Y. Shvartsman. 2014. Vertex models of epithelial morphogenesis. *Biophys. J.* 106:2291–2304. http://dx.doi.org/10.1016/j.bpj.2013.11.4498

Furuse, M., Y. Izumi, Y. Oda, T. Higashi, and N. Iwamoto. 2014. Molecular organization of tricellular tight junctions. *Tissue Barriers.* 2:e28960. http://dx.doi.org/10.4161/tisb.28960

Gumbiner, B., B. Stevenson, and A. Grimaldi. 1988. The role of the cell adhesion molecule uvomorulin in the formation and maintenance of the epithelial junctional complex. *J. Cell Biol.* 107:1575–1587. http://dx.doi.org/10.1083/jcb.107.4.1575

Harris, T.J., and U. Tepass. 2010. Adherens junctions: From molecules to morphogenesis. *Nat. Rev. Mol. Cell Biol.* 11:502–514. http://dx.doi.org/10.1038/nrm2927

Hartman, S.C., and R.C. Mulligan. 1988. Two dominant-acting selectable markers for gene transfer studies in mammalian cells. *Proc. Natl. Acad. Sci. USA.* 85:8047–8051. http://dx.doi.org/10.1073/pnas.85.21.8047

Hoshino, T., T. Sakisaka, T. Baba, T. Yamada, T. Kimura, and Y. Takai. 2005. Regulation of E-cadherin endocytosis by nectin through afadin, Rap1, and p120ctn. *J. Biol. Chem.* 280:24095–24103. http://dx.doi.org/10.1074/jbc.M414447200

Ikeda, W., H. Nakanishi, J. Miyoshi, K. Mandai, H. Ishizaki, M. Tanaka, A. Togawa, K. Takahashi, H. Nishioka, H. Yoshida, et al. 1999. Afadin: A key molecule essential for structural organization of cell-cell junctions of polarized epithelia during embryogenesis. *J. Cell Biol.* 146:1117–1132. http://dx.doi.org/10.1083/jcb.146.5.1117

Ikenouchi, J., K. Umeda, S. Tsukita, M. Furuse, and S. Tsukita. 2007. Requirement of ZO-1 for the formation of belt-like adherens junctions during epithelial cell polarization. *J. Cell Biol.* 176:779–786. http://dx.doi.org/10.1083/jcb.200612080

Ishiuchi, T., and M. Takeichi. 2011. Willin and Par3 cooperatively regulate epithelial apical constriction through aPKC-mediated ROCK phosphorylation. *Nat. Cell Biol.* 13:860–866. http://dx.doi.org/10.1038/ncb2274

Julian, L., and M.F. Olson. 2014. Rho-associated coiled-coil containing kinases (ROCK): Structure, regulation, and functions. *Small GTPases.* 5:e29846. http://dx.doi.org/10.4161/sgtp.29846

Kiehart, D.P., C.G. Galbraith, K.A. Edwards, W.L. Rickoll, and R.A. Montague. 2000. Multiple forces contribute to cell sheet morphogenesis for dorsal closure in *Drosophila*. *J. Cell Biol.* 149:471–490. http://dx.doi.org/10.1083/jcb.149.2.471

Leerberg, J.M., G.A. Gomez, S. Verma, E.J. Moussa, S.K. Wu, R. Priya, B.D. Hoffman, C. Grashoff, M.A. Schwartz, and A.S. Yap. 2014. Tension-sensitive actin assembly supports contractility at the epithelial zonula adherens. *Curr. Biol.* 24:1689–1699. http://dx.doi.org/10.1016/j.cub.2014.06.028

Levayer, R., and T. Lecuit. 2012. Biomechanical regulation of contractility: Spatial control and dynamics. *Trends Cell Biol.* 22:61–81. http://dx.doi.org/10.1016/j.tcb.2011.10.001

Mandai, K., H. Nakanishi, A. Satoh, H. Obaishi, M. Wada, H. Nishioka, M. Itoh, A. Mizoguchi, T. Aoki, T. Fujimoto, et al. 1997. Afadin: A novel actin filament-binding protein with one PDZ domain localized at cadherin-based cell-to-cell adherens junction. *J. Cell Biol.* 139:517–528. http://dx.doi.org/10.1083/jcb.139.2.517

Martin, A.C., M. Kaschube, and E.F. Wieschaus. 2009. Pulsed contractions of an actin-myosin network drive apical constriction. *Nature.* 457:495–499. http://dx.doi.org/10.1038/nature07522

Martin, A.C., M. Gelbart, R. Fernandez-Gonzalez, M. Kaschube, and E.F. Wieschaus. 2010. Integration of contractile forces during tissue invagination. *J. Cell Biol.* 188:735–749. http://dx.doi.org/10.1083/jcb.200910099

Meng, W., and M. Takeichi. 2009. Adherens junction: Molecular architecture and regulation. *Cold Spring Harb. Perspect. Biol.* 1:a002899. http://dx.doi.org/10.1101/cshperspect.a002899

Miyamoto, H., I. Nihonmatsu, S. Kondo, R. Ueda, S. Togashi, K. Hirata, Y. Ikegami, and D. Yamamoto. 1995. *canoe* encodes a novel protein containing a GLGF/DHR motif and functions with *Notch* and *scabrous* in common developmental pathways in *Drosophila. Genes Dev.* 9:612–625. http://dx.doi.org/10.1101/gad.9.5.612

Monteiro, A.C., R. Sumagin, C.R. Rankin, G. Leoni, M.J. Mina, D.M. Reiter, T. Stehle, T.S. Dermody, S.A. Schaefer, R.A. Hall, et al. 2013. JAM-A associates with ZO-2, afadin, and PDZ-GEF1 to activate Rap2c and regulate epithelial barrier function. *Mol. Biol. Cell.* 24:2849–2860. http://dx.doi.org/10.1091/mbc.E13-06-0298

Munro, E., J. Nance, and J.R. Priess. 2004. Cortical flows powered by asymmetrical contraction transport PAR proteins to establish and maintain anterior-posterior polarity in the early *C. elegans* embryo. *Dev. Cell.* 7:413–424. http://dx.doi.org/10.1016/j.devcel.2004.08.001

Nakajima, H., and T. Tanoue. 2010. Epithelial cell shape is regulated by Lulu proteins via myosin-II. *J. Cell Sci.* 123:555–566. http://dx.doi.org/10.1242/jcs.057752

Nakajima, H., and T. Tanoue. 2011. Lulu2 regulates the circumferential actomyosin tensile system in epithelial cells through p114RhoGEF. *J. Cell Biol.* 195:245–261. http://dx.doi.org/10.1083/jcb.201104118

Nakajima, H., and T. Tanoue. 2012. The circumferential actomyosin belt in epithelial cells is regulated by the Lulu2-p114RhoGEF system. *Small GTPases.* 3:91–96. http://dx.doi.org/10.4161/sgtp.19112

Nakata, S., N. Fujita, Y. Kitagawa, R. Okamoto, H. Ogita, and Y. Takai. 2007. Regulation of platelet-derived growth factor receptor activation by afadin through SHP-2: Implications for cellular morphology. *J. Biol. Chem.* 282:37815–37825. http://dx.doi.org/10.1074/jbc.M707461200

Nishimura, T., and M. Takeichi. 2008. Shroom3-mediated recruitment of Rho kinases to the apical cell junctions regulates epithelial and neuroepithelial planar remodeling. *Development.* 135:1493–1502. http://dx.doi.org/10.1242/dev.019646

Ojakian, G.K., and R. Schwimmer. 1988. The polarized distribution of an apical cell surface glycoprotein is maintained by interactions with the cytoskeleton of Madin-Darby canine kidney cells. *J. Cell Biol.* 107:2377–2387. http://dx.doi.org/10.1083/jcb.107.6.2377

Ooshio, T., R. Kobayashi, W. Ikeda, M. Miyata, Y. Fukumoto, N. Matsuzawa, H. Ogita, and Y. Takai. 2010. Involvement of the interaction of afadin with ZO-1 in the formation of tight junctions in Madin-Darby canine kidney cells. *J. Biol. Chem.* 285:5003–5012. http://dx.doi.org/10.1074/jbc.M109.043760

Quinlan, M.P., and J.L. Hyatt. 1999. Establishment of the circumferential actin filament network is a prerequisite for localization of the cadherin-catenin complex in epithelial cells. *Cell Growth Differ.* 10:839–854.

Roh-Johnson, M., G. Shemer, C.D. Higgins, J.H. McClellan, A.D. Werts, U.S. Tulu, L. Gao, E. Betzig, D.P. Kiehart, and B. Goldstein. 2012. Triggering a cell shape change by exploiting preexisting actomyosin contractions. *Science.* 335:1232–1235. http://dx.doi.org/10.1126/science.1217869

Sawyer, J.K., N.J. Harris, K.C. Slep, U. Gaul, and M. Peifer. 2009. The *Drosophila* afadin homologue Canoe regulates linkage of the actin cytoskeleton to adherens junctions during apical constriction. *J. Cell Biol.* 186:57–73. http://dx.doi.org/10.1083/jcb.200904001

Sawyer, J.K., W. Choi, K.C. Jung, L. He, N.J. Harris, and M. Peifer. 2011. A contractile actomyosin network linked to adherens junctions by Canoe/afadin helps drive convergent extension. *Mol. Biol. Cell.* 22:2491–2508. http://dx.doi.org/10.1091/mbc.E11-05-0411

Simões, S.M., A. Mainieri, and J.A. Zallen. 2014. Rho GTPase and Shroom direct planar polarized actomyosin contractility during convergent extension. *J. Cell Biol.* 204:575–589. http://dx.doi.org/10.1083/jcb.201307070

Solon, J., A. Kaya-Copur, J. Colombelli, and D. Brunner. 2009. Pulsed forces timed by a ratchet-like mechanism drive directed tissue movement during dorsal closure. *Cell.* 137:1331–1342. http://dx.doi.org/10.1016/j.cell.2009.03.050

Sumigray, K.D., H.P. Foote, and T. Lechler. 2012. Noncentrosomal microtubules and type II myosins potentiate epidermal cell adhesion and barrier formation. *J. Cell Biol.* 199:513–525. http://dx.doi.org/10.1083/jcb.201206143

Surcel, A., Y.S. Kee, T. Luo, and D.N. Robinson. 2010. Cytokinesis through biochemical-mechanical feedback loops. *Semin. Cell Dev. Biol.* 21:866–873. http://dx.doi.org/10.1016/j.semcdb.2010.08.003

Sveen, J.K.2004 An introduction to MatPIV (Mechanics and Applied Mathematics no. 2). https://www.mn.uio.no/math/english/people/aca/jks/matpiv/ (accessed December 4, 2015).

Takai, Y., W. Ikeda, H. Ogita, and Y. Rikitake. 2008. The immunoglobulin-like cell adhesion molecule nectin and its associated protein afadin. *Annu. Rev. Cell Dev. Biol.* 24:309–342. http://dx.doi.org/10.1146/annurev.cellbio.24.110707.175339

Tanaka-Okamoto, M., K. Hori, H. Ishizaki, Y. Itoh, S. Onishi, S. Yonemura, Y. Takai, and J. Miyoshi. 2011. Involvement of afadin in barrier function and homeostasis of mouse intestinal epithelia. *J. Cell Sci.* 124:2231–2240. http://dx.doi.org/10.1242/jcs.081000

Van Itallie, C.M., A.S. Fanning, A. Bridges, and J.M. Anderson. 2009. ZO-1 stabilizes the tight junction solute barrier through coupling to the perijunctional cytoskeleton. *Mol. Biol. Cell.* 20:3930–3940. http://dx.doi.org/10.1091/mbc.E09-04-0320

Vedula, S.R., M.C. Leong, T.L. Lai, P. Hersen, A.J. Kabla, C.T. Lim, and B. Ladoux. 2012. Emerging modes of collective cell migration induced by geometrical constraints. *Proc. Natl. Acad. Sci. USA.* 109:12974–12979. http://dx.doi.org/10.1073/pnas.1119313109

Vichas, A., and J.A. Zallen. 2011. Translating cell polarity into tissue elongation. *Semin. Cell Dev. Biol.* 22:858–864. http://dx.doi.org/10.1016/j.semcdb.2011.09.013

Yang, Z., S. Zimmerman, P.R. Brakeman, G.M. Beaudoin III, L.F. Reichardt, and D.K. Marciano. 2013. De novo lumen formation and elongation in the developing nephron: A central role for afadin in apical polarity. *Development.* 140:1774–1784. http://dx.doi.org/10.1242/dev.087957

Yao, M., W. Qiu, R. Liu, A.K. Efremov, P. Cong, R. Seddiki, M. Payre, C.T. Lim, B. Ladoux, R.M. Mège, and J. Yan. 2014. Force-dependent conformational switch of α-catenin controls vinculin binding. *Nat. Commun.* 5:4525. http://dx.doi.org/10.1038/ncomms5525

Yonemura, S., Y. Wada, T. Watanabe, A. Nagafuchi, and M. Shibata. 2010. alpha-Catenin as a tension transducer that induces adherens junction development. *Nat. Cell Biol.* 12:533–542. http://dx.doi.org/10.1038/ncb2055

Zehnder, S.M., M.K. Wiatt, J.M. Uruena, A.C. Dunn, W.G. Sawyer, and T.E. Angelini. 2015. Multicellular density fluctuations in epithelial monolayers. *Phys. Rev. E Stat. Nonlin. Soft Matter Phys.* 92:032729. http://dx.doi.org/10.1103/PhysRevE.92.032729

Zhadanov, A.B., D.W. Provance Jr., C.A. Speer, J.D. Coffin, D. Goss, J.A. Blixt, C.M. Reichert, and J.A. Mercer. 1999. Absence of the tight junctional protein AF-6 disrupts epithelial cell-cell junctions and cell polarity during mouse development. *Curr. Biol.* 9:880–888. http://dx.doi.org/10.1016/S0960-9822(99)80392-3

Zhang, L., F. Jouret, J. Rinehart, J. Sfakianos, I. Mellman, R.P. Lifton, L.H. Young, and M.J. Caplan. 2011. AMP-activated protein kinase (AMPK) activation and glycogen synthase kinase-3β (GSK-3β) inhibition induce Ca2+-independent deposition of tight junction components at the plasma membrane. *J. Biol. Chem.* 286:16879–16890. http://dx.doi.org/10.1074/jbc.M110.186932